Check for updates

Received: 30 July 2022 | Revised: 8 December 2022 | Accepted: 5 January 2023

DOI: 10.1111/gbi.12544

gebiology WILEY

ORIGINAL ARTICLE

Organic preservation of vase-shaped microfossils from the late Tonian Chuar Group, Grand Canyon, Arizona, USA

Kelly E. Tingle[1] | Susannah M. Porter[1] | Morgan R. Raven[1] | Andrew D. Czaja[2] | Samuel M. Webb[3] | Bonnie Bloeser[4]

[1]Department of Earth Science, University of California, Santa Barbara, California, USA

[2]Department of Geology, University of Cincinnati, Cincinnati, Ohio, USA

[3]Stanford Synchrotron Radiation Lightsource, Stanford University, Menlo Park, California, USA

[4]Department of Geological Sciences, San Diego State University, San Diego, California, USA

Correspondence
Kelly E. Tingle, Department of Earth Science, University of California, Santa Barbara, California, USA.
Email: kelly.e.tingle@vanderbilt.edu

Present address
Kelly E. Tingle, Department of Earth and Environmental Sciences, Vanderbilt University, Nashville, Tennessee, USA

Funding information
Clay Minerals Society; National Science Foundation, Grant/Award Number: EAR-1855092 and EAR-2029521; University of California, Santa Barbara; NASA; U.S. Department of Energy, Grant/Award Number: DE-AC02-76SF00515; National Institutes of Health, Grant/Award Number: P30GM133894; National Institute of General Medical Sciences

Abstract

Vase-shaped microfossils (VSMs) are found globally in middle Neoproterozoic (800–730 Ma) marine strata and represent the earliest evidence for testate (shell-forming) amoebozoans. VSM tests are hypothesized to have been originally organic in life but are most commonly preserved as secondary mineralized casts and molds. A few reports, however, suggest possible organic preservation. Here, we test the hypothesis that VSMs from shales of the lower Walcott Member of the Chuar Group, Grand Canyon, Arizona, contain original organic material, as reported by B. Bloeser in her pioneering studies of Chuar VSMs. We identified VSMs from two thin section samples of Walcott Member black shales in transmitted light microscopy and used scanning electron microscopy to image VSMs. Carbonaceous material is found within the internal cavity of all VSM tests from both samples and is interpreted as bitumen mobilized from Walcott shales likely during the Cretaceous. Energy dispersive X-ray spectroscopy (EDS) and wavelength dispersive X-ray spectroscopy (WDS) reveal that VSM test walls contain mostly carbon, iron, and sulfur, while silica is present only in the surrounding matrix. Raman spectroscopy was used to compare the thermal maturity of carbonaceous material within the samples and indicated the presence of pyrite and jarosite within fossil material. X-ray absorption spectroscopy revealed the presence of reduced organic sulfur species within the carbonaceous test walls, the carbonaceous material found within test cavities, and in the sedimentary matrix, suggesting that organic matter sulfurization occurred within the Walcott shales. Our suite of spectroscopic analyses reveals that Walcott VSM test walls are organic and sometimes secondarily pyritized (with the pyrite variably oxidized to jarosite). Both preservation modes can occur at a millimeter spatial scale within sample material, and at times even within a single specimen. We propose that sulfurization within the Walcott Shales promoted organic preservation, and furthermore, the ratio of iron to labile VSM organic material controlled the extent of pyrite replacement. Based on our evidence, we conclude that the VSMs are preserved with original organic test material, and speculate that organic VSMs may often go unrecognized, given their light-colored, translucent appearance in transmitted light.

This is an open access article under the terms of the Creative Commons Attribution-NonCommercial-NoDerivs License, which permits use and distribution in any medium, provided the original work is properly cited, the use is non-commercial and no modifications or adaptations are made.
© 2023 The Authors. *Geobiology* published by John Wiley & Sons Ltd.

14724669, 0, Downloaded from https://onlinelibrary.wiley.com/doi/10.1111/gbi.12544 by University Of California, Santa Barbara, Wiley Online Library on [01/03/2023]. See the Terms and Conditions (https://onlinelibrary.wiley.com/terms-and-conditions) on Wiley Online Library for rules of use; OA articles are governed by the applicable Creative Commons License

KEYWORDS
amoebozoa, Chuar Group, Neoproterozoic, organic preservation, pyrite, testate amoebae, Tonian, vase-shaped microfossils

1 | INTRODUCTION

Vase-shaped microfossils (VSMs) are early eukaryotic microfossils found in often exceptional abundances in late Tonian (800–730 Ma) marine strata around the world. They occur as typically flask-shaped or hemispherical tests, ~40 to 300 μm in length, and are interpreted as the oldest fossil evidence for arcellinids, a modern group of testate (shell-forming) amoebozoans that are common today in freshwater habitats, including soils and mosses (Lahr et al., 2019; Meisterfeld, 2000; Porter et al., 2003; Porter & Knoll, 2000; Porter & Riedman, 2019). (A euglyphid [rhizarian] affinity, suggested by Porter and Knoll [2000] and Porter et al. [2003] for some VSM species, seems unlikely given the much younger molecular clock estimates for the origin of that group [Berney & Pawlowski, 2006].) VSMs are found in a variety of rock types, including shales, bedded carbonates—both silicified and non-silicified—and carbonate and phosphate nodules, and are preserved in a variety of ways, including siliceous (Cohen et al., 2017; Fairchild et al., 1978; Green et al., 1988; Knoll et al., 1991; Knoll & Calder, 1983; Morais et al., 2017; Porter & Knoll, 2000; Saito et al., 1988; Sergeev & Schopf, 2010; Strauss et al., 2014), calcareous (Binda & Bokhari, 1980; Cohen et al., 2017; Knoll & Calder, 1983; Strauss et al., 2014), phosphatic (Martí Mus & Moczydłowska, 2000), pyritic or iron oxide (Martí Mus et al., 2020; Morais et al., 2021; Riedman et al., 2018) casts, sometimes with pyrite internal molds (Kraskov, 1985; Martí Mus et al., 2020; Riedman et al., 2018), coatings of pyrite, iron oxide, or organic residue (Binda & Bokhari, 1980; Green et al., 1988; Porter & Knoll, 2000; Strauss et al., 2014) or clay mineralization (Cohen et al., 2017; Martí Mus & Moczydłowska, 2000). Given the variety of taphonomic pathways observed, workers have hypothesized that VSM test material was originally organic (e.g., Bloeser, 1985; Porter & Knoll, 2000; Porter et al., 2003; though see Morais et al., 2017), which is consistent with ancestral state reconstructions of arcellinid test composition (Lahr et al., 2019; Porter & Riedman, 2019). While there are reports of VSMs preserved with organic test walls (Bloeser, 1985; Cohen et al., 2017; Horodyski, 1993; Knoll et al., 1991; Knoll & Calder, 1983; Morais et al., 2017; Riedman et al., 2018; Vidal, 1979), only those by Morais et al. (2017) and Cohen et al. (2017) have been confirmed through compositional analyses.

Here, we report the results of a restudy of VSMs from shales of the lower Walcott Member, Chuar Group, that were originally studied by Bloeser (1985). She interpreted the VSMs to be preserved with their original organic walls, based on electron probe microanalysis showing the presence of carbon in the wall. However, Porter and Knoll (2000) instead suggested these were siliceous casts that were coated internally and externally with organic residue, consistent with the translucent appearance of the wall under transmitted light (Figure 1b; see also Figure 3j,k). We confirm here that Bloeser's specimens are in fact preserved with their original organic walls. We propose that these VSMs were preserved as a result of sulfurization of the organic test material in sulfide-rich (i.e., euxinic) and iron-poor conditions, which is in contrast to ideal conditions for organic-walled microfossil (OWM) preservation (Nagy et al., 2009; Woltz et al., 2021). Thus, organic VSMs may require a different taphonomic window and target rock type (high vs. low total organic carbon content) than OWMs.

2 | GEOLOGIC SETTING

The Chuar Group is a ~2000 m thick succession of siltstone and mudstone interbedded with sandstone and dolomite (Dehler et al., 2001, 2017; Ford & Breed, 1973) deposited in an extensional cratonic basin formed during the rifting of Rodinia (Karlstrom et al., 2000; Timmons et al., 2001, 2005). Exceptionally well-preserved Chuar Group strata are exposed along the western bank of the Colorado River in a 150-km^2 area of the eastern Grand Canyon, Arizona (Figure 2a). The unit is disconformably overlain by the Cambrian-aged Sixtymile Formation (Dehler et al., 2017; Ford & Breed, 1973; Karlstrom et al., 2018), and unconformably overlies the Mesoproterozoic Unkar Group. The Chuar Basin is believed to have formed in an epeiric sea in conjunction with the Pahrump Group basin, California, and the Uinta Mountain Group basin, Utah (Dehler et al., 2017). Paleomagnetic data from the upper Galeros Formation and the Kwagunt Formation indicate deposition in tropical latitudes (Eyster et al., 2020; Weil et al., 2004)

2.1 | Lithology and paleoenvironment

The Chuar Group is divided in ascending order into the Nankoweap, Galeros, and Kwagunt formations (Figure 2b; Dehler et al., 2017; Ford & Breed, 1973), the last of which contains VSM-bearing rocks. The Nankoweap Formation consists of clast-supported conglomerates, containing clasts of basalt and silica-filled amygdules with red and pink sandstone debris, which are overlain by medium- to coarse-grain sandstones interbedded with siltstones and shales (Dehler et al., 2017; Van Gundy, 1951). The Galeros Formation comprises, in ascending order, the Tanner, Jupiter, Carbon Canyon, and Duppa members and is a series of meter-scale cycles of mudrocks, siltstones, and sandstones, frequently capped by dolomite beds (Dehler et al., 2001; Ford & Breed, 1973). Dolomite is prominent in the Tanner and Jupiter Members, both of which are defined by thick (meter-scale) basal (stromatolitic in the case of the Jupiter Member) dolostone beds, and in the Carbon Canyon Member, which contains stromatolite bioherms. Shales in the Galeros Formation typically display a wide range of colors including grey,

14724669, 0, Downloaded from https://onlinelibrary.wiley.com/doi/10.1111/gbi.12544 by University Of California, Santa Barbara, Wiley Online Library on [01/03/2023]. See the Terms and Conditions (https://onlinelibrary.wiley.com/terms-and-conditions) on Wiley Online Library for rules of use; OA articles are governed by the applicable Creative Commons License

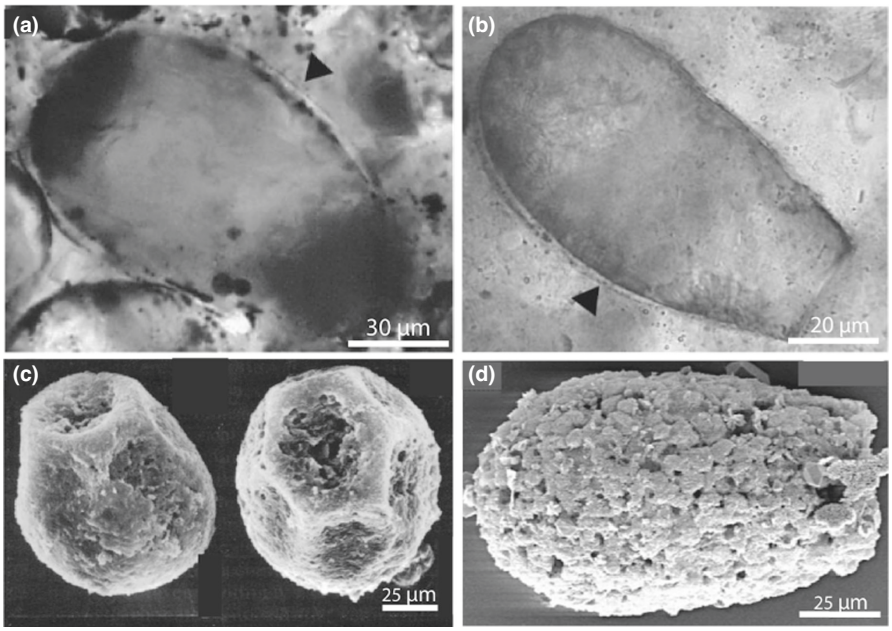

FIGURE 1 Preservation modes of Chuar Group vase-shaped microfossils (VSMs). (a) VSMs in dolomite nodules from the upper Walcott Member reported as siliceous or calcareous casts thinly coated with pyrite or iron oxide. (b) VSM from a shale sample collected by Bruce Runnegar near the same site from which Bloeser's (1985) material came, interpreted by Porter and Knoll (2000; figure 7C), possibly erroneously, to be a siliceous cast coated both internally and externally by exogenous organic debris. (c) VSMs from the lower Walcott Member reported by Bloeser (1985) as organically-preserved tests. (d) A VSM from upper Awatubi Member shales interpreted as a siliceous cast, displaying an agglutinated texture (Porter & Knoll, 2000; figure 7D; Porter & Riedman, 2019). Here, we test the hypothesis that VSMs from lower Walcott Member shales are preserved as original organic tests. (a, b and d) Susannah M. Porter and Andrew H. Knoll, Testate amoebae in the Neoproterozoic Era: Evidence from vase-shaped microfossils in the Chuar Group, Grand Canyon, Paleobiology, volume 26, issue number 3, pages 360–386, 2000, reproduced with permission. (c) Used with permission of Society for Sedimentary Geology (SEPM) from *Melanocyrillium*, a new genus of structurally complex late Proterozoic microfossils from the Kwagunt Formation (Chuar Group), Grand Canyon, Arizona, Bonnie Bloeser, volume 59, issue number 3, 1985; permission conveyed through Copyright Clearance Center, Inc.

green, red, and purple (Ford & Breed, 1973). The Kwagunt Formation is composed of, in ascending order, the Carbon Butte, Awatubi, and Walcott members. The Carbon Butte Member consists primarily of sandstone with interbedded carbonates and, locally, ironstones at its base (Wang et al., 2022). Conspicuous stromatolitic bioherms are found at the base of the Awatubi Member, which are followed by grey, green, and black organic-rich siltstones and shales, some of which contain marcasite nodules. The Walcott Member is characterized by a basal meter-scale laminated dolomite bed ("Flakey Dolomite", Ford & Breed, 1973), overlain by silicified oolites, chert beds, black shales, and in the upper Walcott, a pair of meter-scale dolomite beds (upper and lower dolomite couplet, Dehler et al., 2001) and early diagenetic dolomite nodules up to 1 m in diameter (Dehler et al., 2001, 2017; Ford & Breed, 1973; Porter & Knoll, 2000).

The varying facies of the Chuar Group record fluctuations in sea level, from intertidal or supratidal to subtidal paleoenvironments (Dehler et al., 2001). Some facies include features consistent with intermittent desiccation, such as exposure surfaces and red beds, along with evidence in the Carbon Canyon Member for an anomalously high radiogenic Osmium signal, indicative of a relatively high flux of continental derived materials, consistent with deposition in a restricted basin (Dehler et al., 2001; Rooney et al., 2018). It is likely, however, that the Chuar Basin maintained some marine connection for the majority of its deposition, given the presence of OWMs found elsewhere in marine assemblages (Porter & Knoll, 2000; Porter & Riedman, 2016; Vidal & Ford, 1985) and–especially in upper Chuar rocks–the high pyrite content (Ford & Breed, 1973; Porter & Knoll, 2000); marine settings, unlike lacustrine settings which are typically sulfate depleted (Berner & Raiswell, 1983), tend to have high concentrations of iron sulfides. The upper Awatubi Member and Walcott Member record higher amplitude sea-level changes and contain the deepest water (sub-storm wave-base) facies. Ferruginous conditions were prevalent throughout the majority of Chuar deposition, with evidence of euxinic conditions during Walcott time (Johnston et al., 2010). New iron isotopic data from the Chuar Group provides a direct constraint on atmospheric oxygen during deposition of the upper Duppa and lower Carbon Butte members and suggests that shallow waters of the Chuar Basin were oxygen-rich (Wang et al., 2022).

2.2 | Age

The Nankoweap Formation is constrained to be <782 Ma based on U–Pb dating of detrital zircons from basal beds (Dehler et al., 2017). Re–Os ages from organic-rich carbonates within the upper Galeros Formation and marcasite nodules from the lower Kwagunt

14724669, 0, Downloaded from https://onlinelibrary.wiley.com/doi/10.1111/gbi.12544 by University Of California, Santa Barbara, Wiley Online Library on [01/03/2023]. See the Terms and Conditions (https://onlinelibrary.wiley.com/terms-and-conditions) on Wiley Online Library for rules of use; OA articles are governed by the applicable Creative Commons License

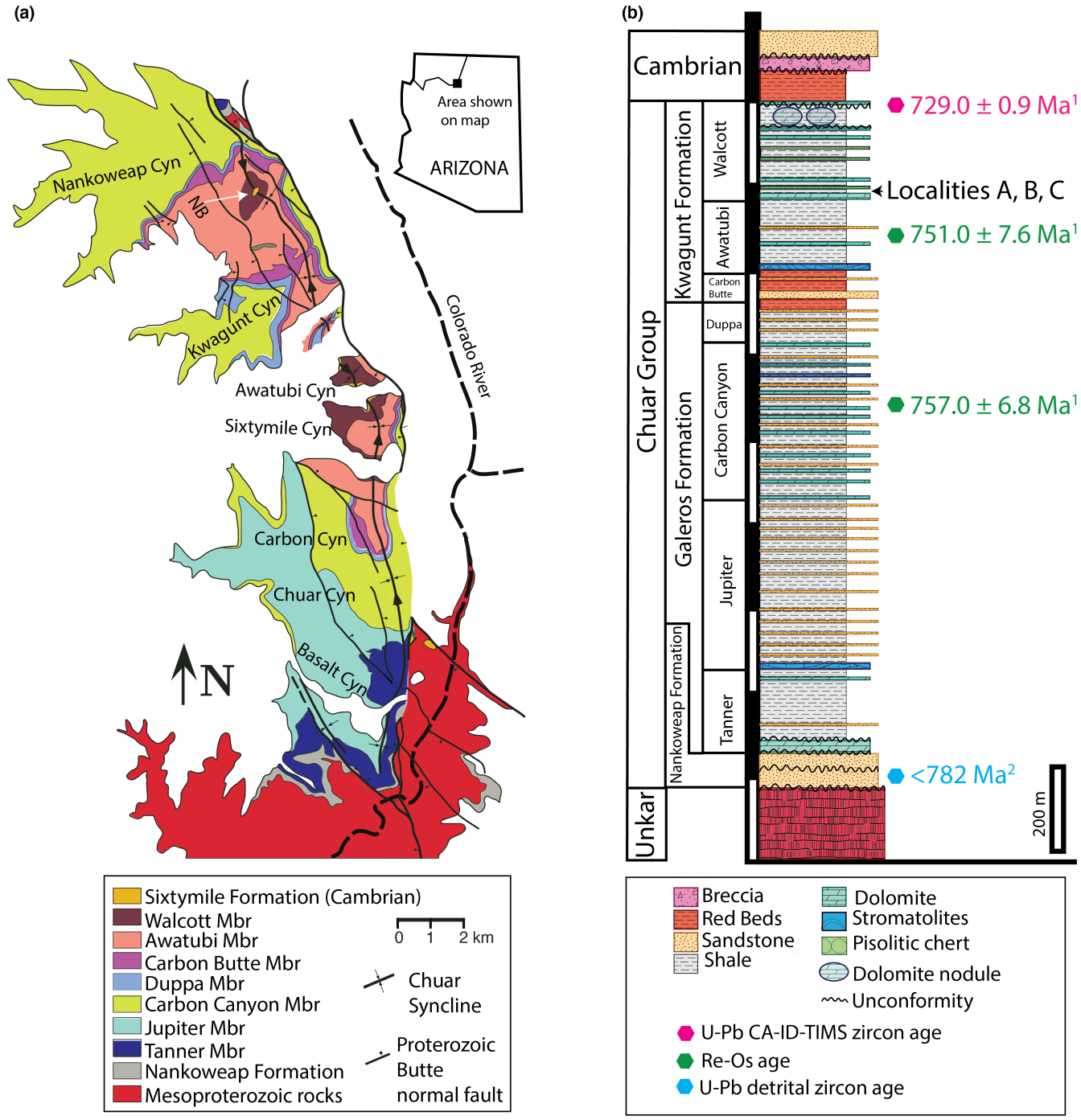

FIGURE 2 Locality and stratigraphic column. (a) Geologic map of the Chuar Group, northeastern Grand Canyon (modified from Timmons et al., 2001). NB, Nankoweap Butte. Vase-shaped microfossils are found in the Walcott Member (brown) and the Awatubi Member (peach). Shale samples for this study were from three localities on and around Nankoweap Butte, at 36°15′50″N and 111°53′22″W (Bloeser, 1985). (b) Stratigraphic section of the Chuar Group, Grand Canyon, Arizona. Redrawn from Dehler et al. (2017). Ages: 1 – Rooney et al. (2018); 2 – Dehler et al. (2017). CA-ID-TIMS, chemical abrasion–isotope dilution–thermal ionization mass spectrometry.

Formation reveal ages of 757.0 ± 6.8 and 751.0 ± 7.6 Ma, respectively (Rooney et al., 2018). The top of the Walcott Member is dated at 729.0 ± 0.9 Ma from a U–Pb chemical abrasion–isotope dilution–thermal ionization mass spectrometry (CA-ID-TIMS) age from zircons recovered from a tuff (Rooney et al., 2018). Thus, the Chuar Group age is well constrained between 729 and 782 Ma, and furthermore the VSM-bearing Walcott Member is between 751 and 729 Ma.

2.3 | Fossil occurrences

The Duppa, Carbon Canyon, Jupiter, and Tanner members of the Chuar Group contains organic-walled microfossils, including filaments, colonial forms, and both smooth-walled and ornamented vesicles (Horodyski, 1993; Horodyski & Bloeser, 1983; Porter

14724669, 0, Downloaded from https://onlinelibrary.wiley.com/doi/10.1111/ghi.12544 by University Of California, Santa Barbara, Wiley Online Library on [01/03/2023]. See the Terms and Conditions (https://onlinelibrary.wiley.com/terms-and-conditions) on Wiley Online Library for rules of use; OA articles are governed by the applicable Creative Commons License

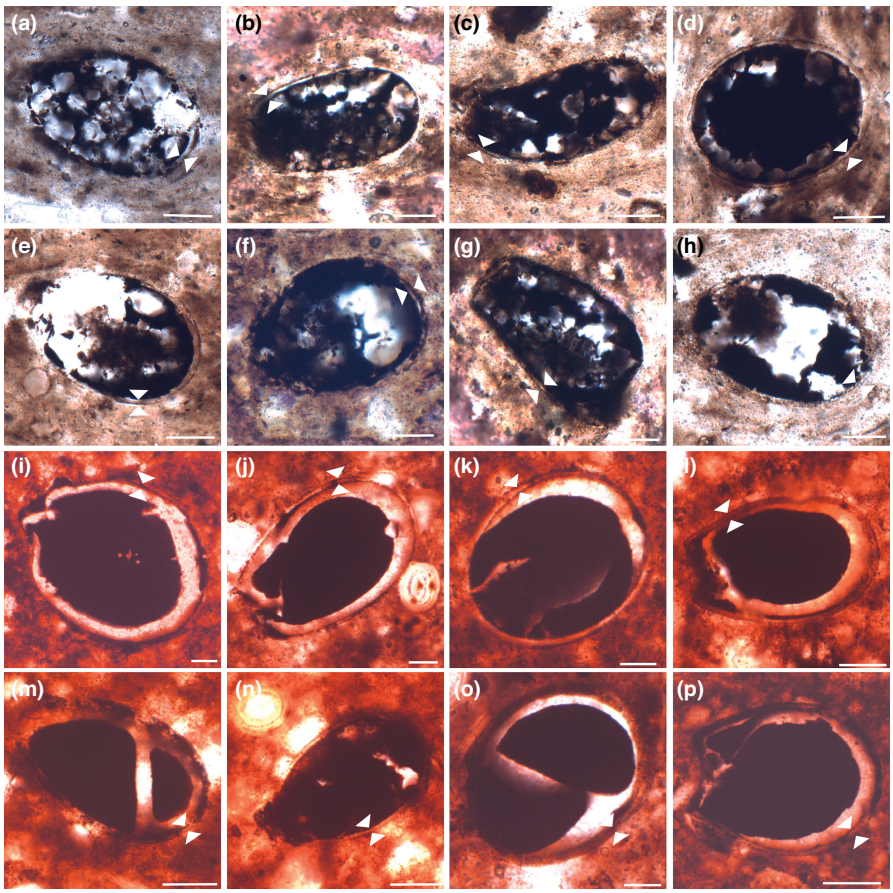

FIGURE 3 Transmitted light photomicrographs of Walcott Shale vase-shaped microfossils (VSMs). VSMs are preserved from sample CS2 as original organic tests (a–h) and from sample CS3 as original organic tests (i–k) and partial or complete pyrite and/or jarosite casts (l–p). Arrow tips point to test walls. All VSMs are infilled with an opaque material which we interpret as bitumen and refer to as exogenous carbonaceous material (ECM) (see text). Note the light, translucent color of VSM walls (between white arrows), distinct from the opaque/black color of the ECM. In sample CS2, ECM exhibits a web-like pattern which is likely the result of flowing around and through a siliceous internal mold. In sample CS3, ECM appears to have filled tests and subsequently shrunk and cracked, often retaining the overall test morphology. a, b, d–h, j–m, o, p, unidentified species; c, *Bonniea dacruchares*; i, n, *Cyclocyrillium torquata*. a, (CS2.1A; S-38/2). b, (CS2.1A; K-51/4). c, (CS2.1A; Q-66/2). d, (CS2.1A; O-52/4). e, (CS2.1A; X-59/3). f, (CS2.1A; G-49/3). g, (CS2.1A; K-51/3). h, (CS2.1A; Y-60). i, (CS3.1; K-51/1). j, (CS3.1; Q-54/4). k, (CS3.1; S-56/2). l, (CS3.1; V-53/3). m, (CS3.1; T-55). n, (CS3.1; U-56/1). o, (CS3.1; Q-42/3). p, (CS3.1; L-45/4). Scale bar = 20 μm.

& Riedman, 2016; Schopf et al., 1973; Vidal & Ford, 1985). In addition to body fossils, stromatolites (Dehler et al., 2001; Ford & Breed, 1973), and biomarkers (Brocks et al., 2016; Summons et al., 1988; Zumberge et al., 2019) are reported. VSMs, which co-occur with the macroscopic organic-walled fossil *Chuaria* (Ford & Breed, 1973; Walcott, 1899) and phosphatic scale microfossils (Riedman et al., 2021), are found only in the Walcott and Awatubi members.

Vase-shaped microfossils first appear in the Kwagunt Formation in upper Awatubi Member shales and are reported as carbonaceous tests and siliceous, possibly agglutinated, casts (Horodyski, 1993; Porter & Knoll, 2000). In the lower Walcott Member, VSMs are reported as carbonaceous tests in shales and as mineralized tests in silicified carbonates (Bloeser et al., 1977; Bloeser, 1985; Porter & Knoll, 2000). In the upper Walcott Member, VSMs are found in dolomite nodules within uppermost Walcott shales in great numbers (up to 4000/mm^3) and are reported as siliceous and calcareous casts and molds, sometimes coated with pyrite or iron oxide (Figure 1a; Morais et al., 2019; Porter & Knoll, 2000; Porter et al., 2003). Whether the carbonaceous VSMs reported from the lower Walcott Shales represent primary organic material has yet to be determined conclusively and is therefore the motivation for this study.

3 | MATERIALS AND METHODS

VSMs were identified in polished thin sections cut perpendicular to bedding from two shale samples (Chuar Shale 2 and Chuar Shale 3 as denoted by B. Bloeser) from the lower Walcott Member, using a Zeiss Axioskop 40 transmitted light microscope. Shale samples–collected by R. Horodyski in the 1970s and given to B. Bloeser–are from three localities (A–C) at 36°15′50″N and 111°53′22″W

14724669, 0, Downloaded from https://onlinelibrary.wiley.com/doi/10.1111/gbi.12544 by University Of California, Santa Barbara, Wiley Online Library on [01/03/2023]. See the Terms and Conditions (https://onlinelibrary.wiley.com/terms-and-conditions) on Wiley Online Library for rules of use; OA articles are governed by the applicable Creative Commons License

(Bloeser, 1985; Bloeser et al., 1977). Locality A occurs ~3 m below the lowermost pisolite bed and above the basal 'flaky' dolomite bed. Locality B and C are located about 450 m apart from one another on the northeast flank of Nankoweap Butte, 1 m below a bed of black chert (see Figure 2b; Bloeser, 1985; figure 1). We do not have records of which shale sample came from which locality. Thin sections and shale samples are in the collections of S. Porter at UCSB. Thin sections are labeled CS2 and CS3, denoting samples Chuar Shale 2 or Chuar Shale 3, with additional numbering (.1, .2, .3) and lettering (A, B) for the purpose of organization; thin sections and England Finder coordinates are noted in parentheses in the figure captions, with slide labels oriented on the left side, opposite the fixed corner. If possible, VSMs were identified to genus and species level and such identifications are specified in the figure captions.

For VSM imaging, thin sections were sputter-coated with a ~3 to 5 nm-thick layer of gold–palladium alloy (80:20) and analyzed with an FEI Quanta 400F field emission source scanning electron microscope (SEM) equipped with an INCAx-act silicon drift detector X-ray energy spectrometer at the Department of Earth Science, University of California, Santa Barbara. The SEM was operated at a working distance of ~10 mm with accelerating voltages between 10 and 15 kV and beam currents of ~0.1 to 1 nA. Secondary electron and backscattered electron signals were acquired to image VSMs and detect qualitative changes in sample mean atomic number (a proxy for chemical compositional variability). Individual 'spot/point' X-ray spectra were gathered from sample volumes of ~1 to 2 μm^3 that accumulated for ~30 s to assess local chemical composition. X-ray intensity maps were created by scanning the electron beam across VSMs and adjacent matrix areas to assess variation in chemical composition.

Elemental spatial variation within VSM tests was assessed with a Cameca SX100 equipped with five wavelength dispersive spectroscopy (WDS) spectrometers at the Department of Earth Science, University of California, Santa Barbara. WDS spectrometers were tuned to the wavelength corresponding to the K-alpha characteristic X-ray emission for the elements Si, C, S, P and Fe. Maps of raw X-ray intensity were assembled by collecting 200 ms of data on a grid pattern with $0.5 \times 0.5\,\mu m^2$ spacing (each map has a different number of x–y pixels). We used 20 nA of beam current, with 15 kV accelerating voltage, and a fully-focused electron beam. WDS elemental maps were processed using ImageJ2 software.

The molecular structure of carbonaceous material within VSM test walls, VSM test interiors, and matrix of Walcott Member samples was measured at the University of Cincinnati, Department of Geology with a Horiba T64000 Raman system (Horiba Inc.) equipped with an Olympus BX41 microscope with a 50× long working distance objective (numerical aperture = 0.50) and 457.9 nm excitation from a Coherent FreD 90C Ar+ laser having a spot size of ~1 μm. We used a neutral density filter to decrease the laser power to 1 mW at the sample and processed the data using the software LabSpec (v.5; Horiba Inc.).

The redox speciation and bonding environments of sulfur and iron in the VSM and matrix material were analyzed at beam line 14–3 at the Stanford Synchrotron Radiation Lightsource (SSRL), which is equipped with a Si(111) (Φ = 90) double crystal monochromator. Energies were calibrated to the thiol pre-edge peak of thiosulfate at 2472.02 eV. The S Kα fluorescence line was measured with a Si Vortex Si drift detector (Hitachi) using Xspress3 pulse processing electronics (Quantum Detectors). The X-ray beam was focused using an axially symmetric focusing mirror (SIGRAY) to a size of 1×1 μm at a flux of $\sim 8 \times 10^{10}$ photons per second. Fossil-bearing regions were mapped using a step size of 1 μm^2 at eight specific energies (2471.0, 2472.8, 2473.5, 2474.1, 2475.8, 2481.1, 2482.5, and 2485.0 eV) to create elemental and chemical distribution maps. Full X-ray absorption (XAS) spectra were then collected from 2460 to 2540 eV at selected spots. Sulfur XAS spectra were processed in the SIXPACK (Webb, 2005) software package using a K-edge E0 of 2473 and pre-edge and post-edge linear normalization ranges of −20 to −7 and 35 to 70 eV, respectively. X-ray fluorescence (XRF) maps were processed using the MicroAnalysis Toolkit (SMAK; Webb et al., 2011). Sulfur X-ray absorption near-edge structure (XANES) fitting used a set of five standard spectra (pyrite, glutathione disulfide, dibenzothiophene (aromatic organic sulfur [OS]), cysteic acid/sulfonate, and inorganic sulfate).

4 | RESULTS

4.1 | Light microscopy

VSMs identified in samples CS2 and CS3 vary in length from 44 to 132 μm (mean = 78 μm; SD = 20 μm; $N = 66$) and in width from 34 to 104 μm (mean = 56 μm; SD = 16 μm; $N = 66$). Test wall thickness varies from 1.2 to 5.6 μm (mean = 2.4 μm; SD = 0.8 μm; $N = 66$) and is correlated with test length (Figure S1). When considering only carbonaceous VSMs (see mineralogy results below), test wall thickness varies from 1.2 to 3.3 μm (mean = 2.0 μm; SD = 0.6 μm; $N = 29$). We identified *Cycliocyrillium torquata* (Figures 3i,n, 4e,i, 5k), *Bonniea dachruchares* (Figures 3c, 4a, 6), and *Bonniea* sp. (Figures 4c,f,g and 5c). *Cycliocyrillium* sp. and *Trigonocyrillium horodyskii* may also be represented within the sample population, but it is difficult to distinguish between the two in transverse section given that they differ only in apertural shape.

In sample CS2, test walls appear translucent in transmitted light (Figure 3a–h) and opaque in reflective light. All VSMs possess a dark-colored material in their test interiors (opaque in transmitted and reflected light) which is variably opaque (compare Figure 3d vs. a). This opaque substance appears to be connected to test walls in a web-like fashion (Figure 3a). Additionally, a lighter-colored material is dispersed inside the tests within this darker material.

In sample CS3, test walls appear either translucent, usually with some mottling (Figure 3j,k) or opaque in transmitted and reflected light (Figure 3o,p). As in sample CS2, all VSMs maintain a dark-colored material inside their tests, but this material appears opaquer and more

14724669, 0, Downloaded from https://onlinelibrary.wiley.com/doi/10.1111/ghi.12544 by University Of California, Santa Barbara, Wiley Online Library on [01/03/2023]. See the Terms and Conditions (https://onlinelibrary.wiley.com/terms-and-conditions) on Wiley Online Library for rules of use; OA articles are governed by the applicable Creative Commons License

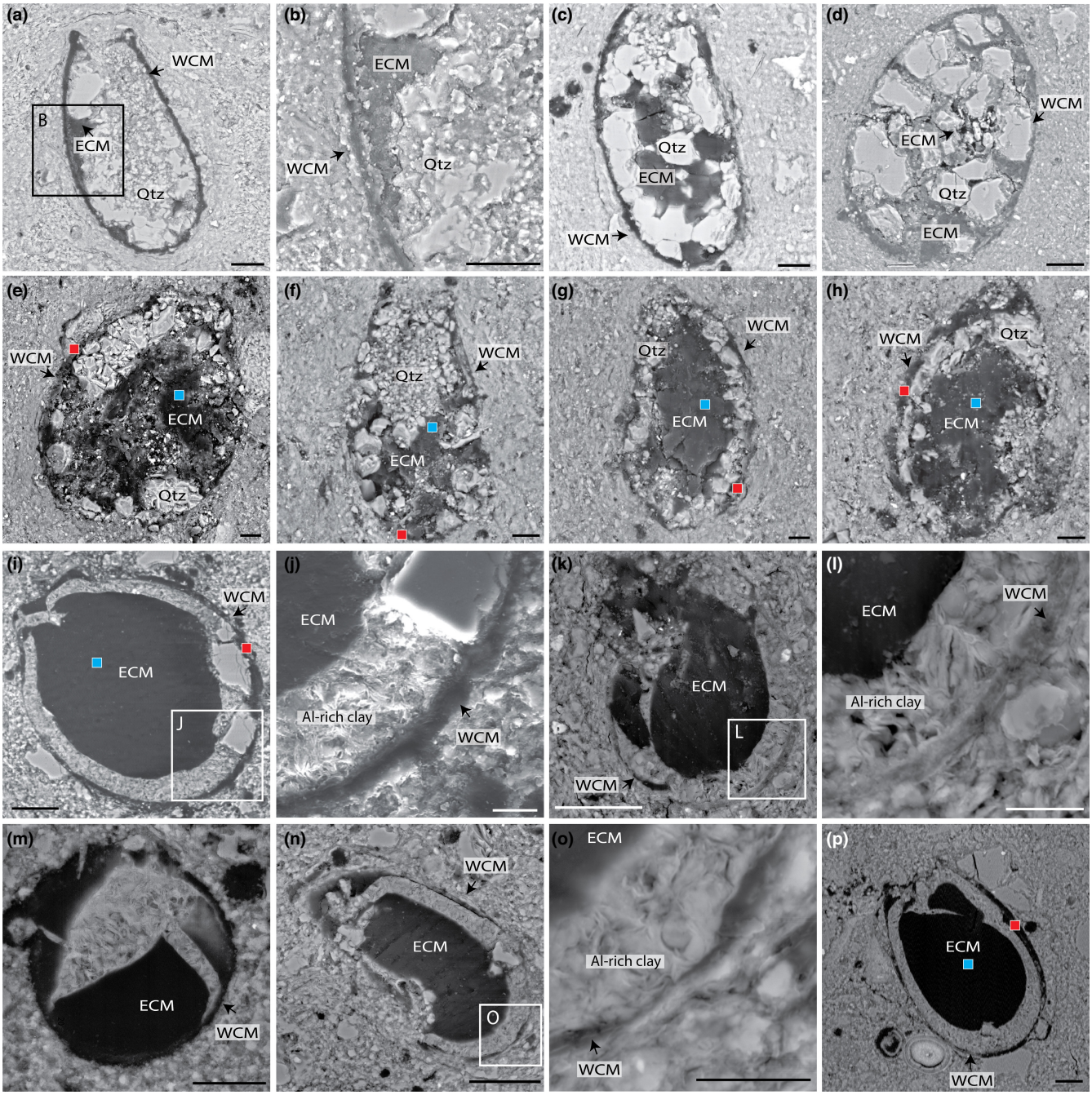

FIGURE 4 Backscattered electron (BSE) images of carbonaceous vase-shaped microfossils (VSMs) from lower Walcott Member shales. ECM, exogenous carbonaceous material; WCM, wall carbonaceous material. VSMs from samples CS2 (a–h) and CS3 (i–p). Note the presence of ECM in all VSMs, and the test wall carbonaceous material (WCM), which is often separated by microcrystalline quart (Qtz) in sample CS2 and Al-rich clay minerals in sample CS3. Blue and red squares indicate areas where Raman spectra was acquired (Figure 8) of ECM and WCM, respectively. (a) *Bonniea dachruchares*; (CS2.1A; H-50/1). (b) A magnification of the area shown in (a). (c) *Bonniea* sp.; (CS2.1A; Q-66/2). (d) (CS2.1A; S-38/2). (e) *Cycliocyrillium torquata*; (CS2.1B; K-55/3). (f) *Bonniea* sp.; (CS2.1B; R-60/3). (g) *Bonniea* sp.; (CS2.1B; U-55/1). (h) (CS2.1B; T-66/4). (i) *Cycliocyrillium torquata*, (CS3.1; K-51/1). (j) Magnification of the region pictured in (i). (k) (CS3.3; S-49/2). (l) Magnification of the region pictured in (k); (CS3.3; S-49/2). (m) (CS3.2; Q-61/4). (n) (CS3.3; L-45/4). (o) Magnification of the region pictured in (n), (CS3.1; Q-54/4). (p) (CS3.1; Q-54/4). Scale bar = 5 μm for b, e, h, 10 μm for a, c, d, f, g, and 20 μm in all other images.

cohesive compared to sample CS2. Moreover, this material seemingly retains the morphology of the overall test shape and shows cracking patterns suggestive of desiccation (Figure 3j,k,m,o,p); these cracks are often filled in by a material that appears bright in transmitted light.

4.2 | Scanning electron microscopy

Energy dispersive X-ray spectroscopy (EDS) spot analyses indicate that test walls of all observed VSMs (n = 20) from sample

14724669, 0, Downloaded from https://onlinelibrary.wiley.com/doi/10.1111/gbi.12544 by University Of California, Santa Barbara, Wiley Online Library on [01/03/2023]. See the Terms and Conditions (https://onlinelibrary.wiley.com/terms-and-conditions) on Wiley Online Library for rules of use; OA articles are governed by the applicable Creative Commons License

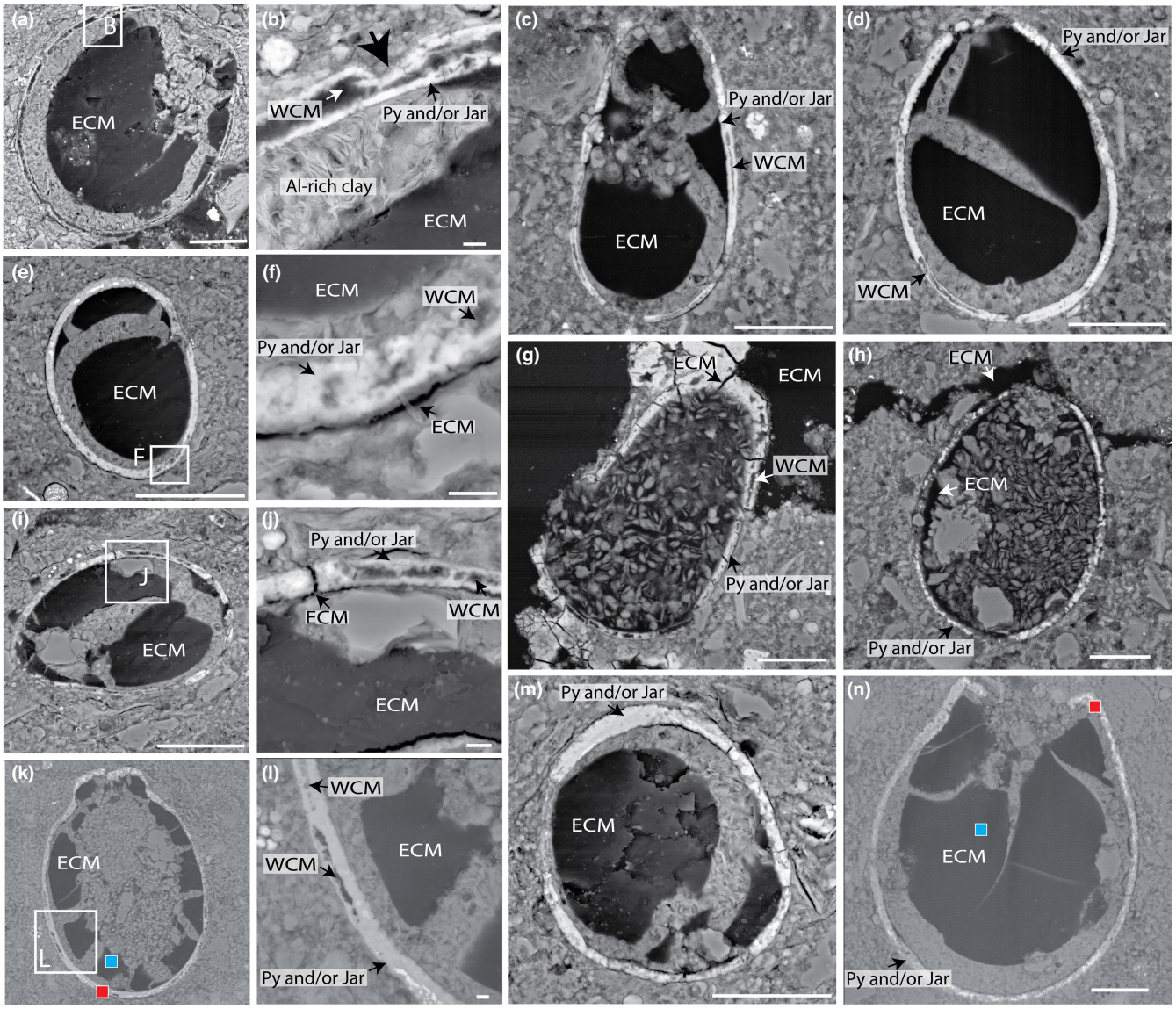

FIGURE 5 Backscattered electron (BSE) images of vase-shaped microfossils (VSMs) from sample CS3 showing partial and complete mineralization. ECM, exogenous carbonaceous material; Jar, jarosite; Py, pyrite; WCM, wall carbonaceous material. Blue and red squares indicate areas Raman spectra was acquired (Figure 8) of ECM and WCM, respectively. Pyrite is the primary mineral that replaced WCM and was later variably oxidized to jarosite. (a) VSM with a partially mineralized carbonaceous test wall; (CS3.3B; Q-55/2). (b) Magnification of area specified in (a). The large black arrow points to an indentation of the mineralized wall, suggesting that replacement occurred early in diagenesis, prior to compaction. Note the presence of platy, Al-rich clay minerals. (c) Partial cast of *Bonniea* sp.; (CS3.2; L-45). (d, e) partial casts (CS3.2; E-49/4; CS3.3; M-46/1). (f) Magnification of the area specified in (e), showing a thin ECM coating on the fossil exterior. (g) Partially mineralized VSM surrounded by a mass of ECM. This VSM was likely filled by ECM through fractures in the test walls; (CS3.2; V-51/4). (h) Mineralized VSM in contact with a vein of ECM (CS3.2; K-56/1). (i) Partially mineralized VSM (CS3.3B; M-44/1). (j) Magnification of area shown in (i). (k) Partially mineralized *Cycliocyrillium torquata*; (CS3.1; Y-40/1). (l) Magnification of region shown in (k). (m) Cast that is likely partly coated, given its non-uniform thickness, (Figure S1) (CS3.3; M-43/3). (n) Complete cast, (CS3.1; L-45/4). Scale bar = 2 μm for b, f, j, l; 25 μm for all other images.

CS2 are predominantly carbon with silicon, oxygen, and minor iron, aluminum, sulfur, magnesium, potassium and chloride. (Table 1, Figure S2). The matrix is enriched in aluminum, silicon, and oxygen. The light-colored material, which occurs within and peripheral to the opaque internal material, is likely microcrystalline quartz based on its chemistry and morphology (Figure 4a–h).The opaque internal material inside the VSMs is principally carbon, with minor amounts of sulfur, aluminum and silicon.

EDS spot analyses of VSMs from sample CS3 revealed two types of test walls. In one type (n = 10), 22% of test walls are mostly carbon, with silicon, oxygen, aluminum, phosphorus, and minor amounts of iron, magnesium, sodium and chloride (Table 1, Figure S3); in the other type (n = 36), 78% of test walls are iron, silicon, aluminum, carbon and sulfur with potassium, phosphorus, and chloride (Table 1, Figure S4). The outer matrix is enriched in silicon relative to the interior of the test (Figures S3 and S4). In the test

14724669, 0, Downloaded from https://onlinelibrary.wiley.com/doi/10.1111/gbi.12544 by University Of California, Santa Barbara, Wiley Online Library on [01/03/2023]. See the Terms and Conditions (https://onlinelibrary.wiley.com/terms-and-conditions) on Wiley Online Library for rules of use; OA articles are governed by the applicable Creative Commons License

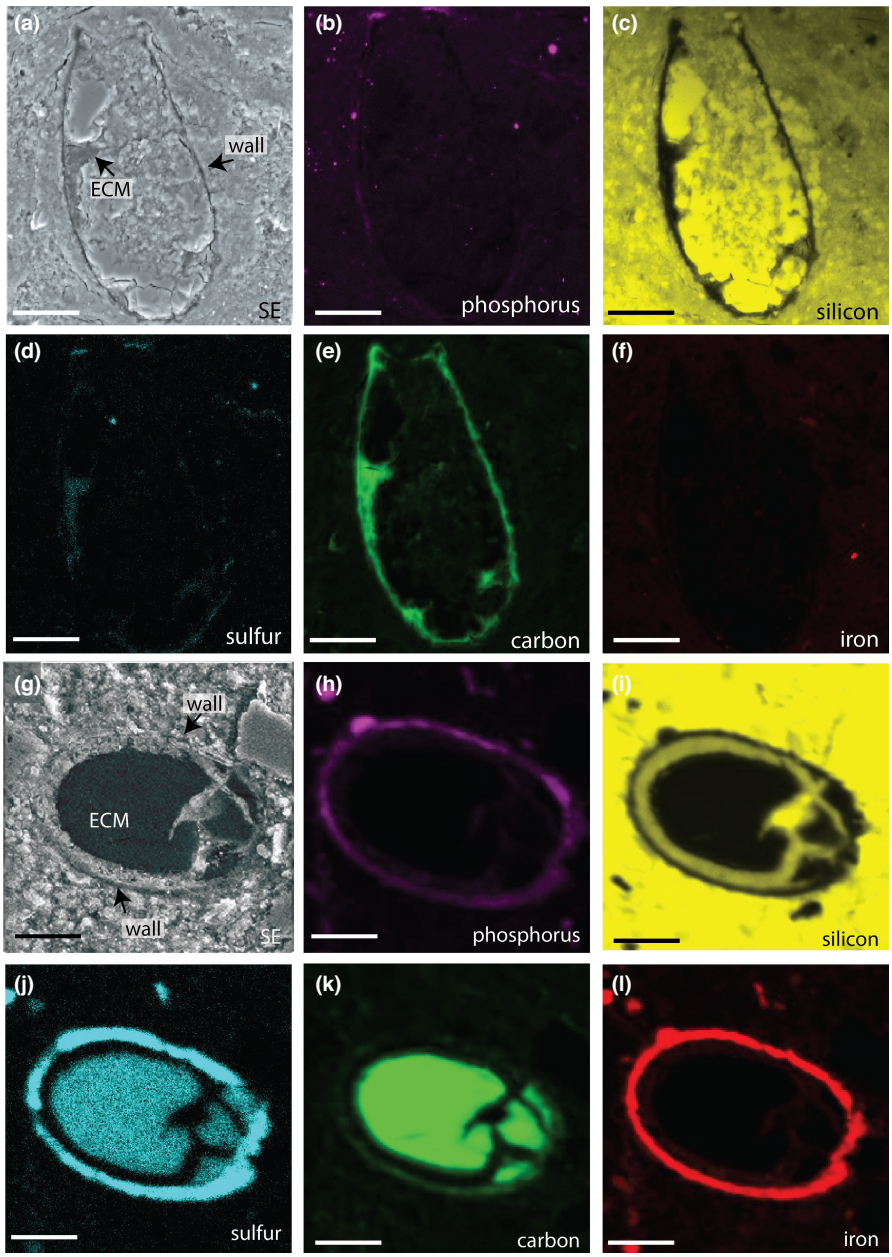

FIGURE 6 Wavelength dispersive spectroscopy (WDS) elemental maps of organically-preserved *Bonniea dachruchares* from sample CS2 (a–f) and mineralized VSM from sample CS3 (g–l). Brightness corresponds to abundance of element; brighter colors indicate higher abundance, darkness indicate absence. Note the absence of silicon in the test walls. (a, g) Secondary electron images. (b, h) Phosphorus. (c, i) Silicon. (d, j) Sulfur. (e, k) Carbon. (f, l) Iron. Scale bars are 20 μm in (a–f), and 15 μm in (g–l). (CS2.1A; H-50/1. CS3.2; Q-62/1).

interiors of all observed VSMs from sample CS3 (n = 46), located around the periphery and within microfractures of the internal carbonaceous material is a platy, microcrystalline Al-rich material, possibly kaolinite or another Al-rich clay mineral phase (Figures S3 and S4, Figures 4j,l,o and 5b). VSMs can also contain isolated crystals of microcrystalline quartz (Figures 4j and 5j). Mineralized coatings are also identified, as at least one test wall appears anomalously thick compared to other observed VSMs (>4 μm, Figure S1; Figure 5m). BSE/SE imaging within seven specimens revealed that the internal carbonaceous material is of two distinct forms within individual microfossils: a large central mass that is often still attached to test walls (Figure 5a,d,e), and a thin (~0.5 μm), darker (in BSE) material that appears cutting across test walls and thinly coating test interiors and exteriors (Figure 5f,j).

4.3 | Electron probe micro-analysis

The electron probe micro-analyzer was employed to gain an improved understanding of the spatial distribution of silicon, carbon, iron, sulfur, and phosphorus. Wavelength dispersive X-ray spectroscopy (WDS) elemental maps illustrate that in sample CS2, test walls contain carbon, sulfur, and phosphorous, and lack silicon (Figure 6a–f). The lack of evidence for silicon from VSM test walls contradicts our findings from EDS spot spectra and likely reflects the greater spatial resolution of EDS relative to WDS. The internal carbonaceous material consists primarily of carbon and sulfur: minor iron, silicon, or phosphorus was detected by WDS. In addition, the matrix of sample CS2 has minor concentrations of iron and phosphorus (Figures 6b,f and 7b). In sample CS3, test walls contain carbon, iron, sulfur, and

14724669, 0, Downloaded from https://onlinelibrary.wiley.com/doi/10.1111/gbi.12544 by University Of California, Santa Barbara, Wiley Online Library on [01/03/2023]. See the Terms and Conditions (https://onlinelibrary.wiley.com/terms-and-conditions) on Wiley Online Library for rules of use; OA articles are governed by the applicable Creative Commons License

TABLE 1 Summary of energy dispersive X-ray spectroscopy (EDS) spot analyses of vase-shaped microfossils (VSMs) from samples CS2 and CS3.

	C	S	Fe	Si	P	Al	O	Mg	K	Cl	Na	Ca
Organic VSM, sample CS2												
Test wall	×	×	×	×		×	×	×	×	×		
ECM	×	×		×		×						
Test interior	×		×	×		×	×	×	×			
Matrix	×		×	×		×	×	×	×			
Organic VSM, sample CS3												
Test wall	×		×	×	×	×	×	×		×	×	
ECM	×	×		×								
Test interior	×		×	×		×	×	×	×			
Matrix			×	×	×	×	×	×	×			×
Mineralized VSM, sample CS3												
Test wall	×		×	×	×	×	×		×	×		
ECM	×	×										
Test interior	×		×	×	×	×	×	×	×			
Matrix	×		×	×	×	×	×	×	×		×	

Note: An '×' indicates presence of an element, with blank squares indicating absence. The relative abundances of elements are illustrated in the full spectra in Figures S2–S4.

Abbreviation: ECM, exogenous carbonaceous material found within VSMs.

phosphorus (Figure 6g–l, Figure S6); silicon was not detected in the test walls. As with sample CS2, the internal carbonaceous material is made of carbon and sulfur. The matrix of sample CS3, in contrast to sample CS2, has high levels of phosphorus (Figures S5 and S6), as well as zones that are iron-enriched and iron-poor (Figure 7).

4.4 | Raman spectroscopy

Mineral identification and thermal maturity of carbonaceous material within the samples was investigated using Raman spectroscopy. The silicon-oxygen mineral in VSMs of sample CS2 is confirmed as quartz (Figure 8) and the iron–sulfur minerals found in the walls of VSMs of sample CS3 are pyrite and jarosite (Figure S9). The internal carbonaceous material and test walls of both samples CS2 and CS3 show prominent D (~1350 cm^{-1}) and G (~1600 cm^{-1}) bands that are similar in shape and intensity, suggesting both are composed of organic matter similar in thermal maturity, although it is not clear from the observed spectra that the internal carbonaceous material and test walls are composed of distinct materials. The Raman spectra of the test walls of sample CS2 are generally noisier with higher background levels compared to the test walls of sample CS3 (Figure 8a,b, Figures S7 and S8).

4.5 | X-ray absorption spectroscopy

X-ray absorption spectroscopy indicated that sulfur species are present in varying oxidation states within the VSMs and the shale matrix of sample CS3. Mineralized test walls (Figure 9a) confirm the presence of inorganic sulfur in both oxidized (sulfate) and reduced (pyrite, pyrrhotite) forms, as well as both oxidized (sulfonate, sulfate esters) and reduced organic sulfur (monosulfide). Carbonaceous test walls (Figure 9b) show both relatively oxidized (sulfoxide, sulfonate) and reduced (disulfide, monosulfide, aromatic) organic sulfur, along with inorganic sulfur (sulfate [30%] and pyrrhotite [10%]). Sulfur speciation of the internal carbonaceous material within the observed VSMs is similar, with more than 60% (fit 1σ uncertainties typ. ±2%) reduced organic sulfur (disulfide, monosulfide, aromatic). Carbonaceous test walls (Figure 9b, spot 14) have a broadly similar speciation to the internal carbonaceous material, although it is distinguished by the presence of FeS (pyrrhotite, 8%) and a slightly elevated contribution (~12% of total S) from organic sulfonates. Sulfur speciation of matrix material is more similar to test walls in Figure 9a and more similar to the internal carbonaceous material in Figure 9b, although it can be distinguished from both by increased contributions of pyrite and structural sulfates (e.g., gypsum or jarosite).

5 | DISCUSSION

5.1 | Exogenous carbonaceous material within the VSM tests: Origin and timing of emplacement

Although it is possible that some of the carbon may have derived from the original cell (Carlisle et al., 2021), it seems unlikely that the total volume of carbon is from the cell alone given (a) the organic-rich matrix of the Walcott shales (>3 wt% TOC, Woltz et al., 2021) and (b) the occurrence of carbonaceous material located adjacent to VSMs, which may continue from the matrix into test interiors via cracks in test walls (Figure 5g,h). Cohen et al. (2017) reported VSMs from the Callison Lake Formation preserved with carbonaceous inclusions

14724669, 0, Downloaded from https://onlinelibrary.wiley.com/doi/10.1111/gbi.12544 by University Of California, Santa Barbara, Wiley Online Library on [01/03/2023]. See the Terms and Conditions (https://onlinelibrary.wiley.com/terms-and-conditions) on Wiley Online Library for rules of use; OA articles are governed by the applicable Creative Commons License

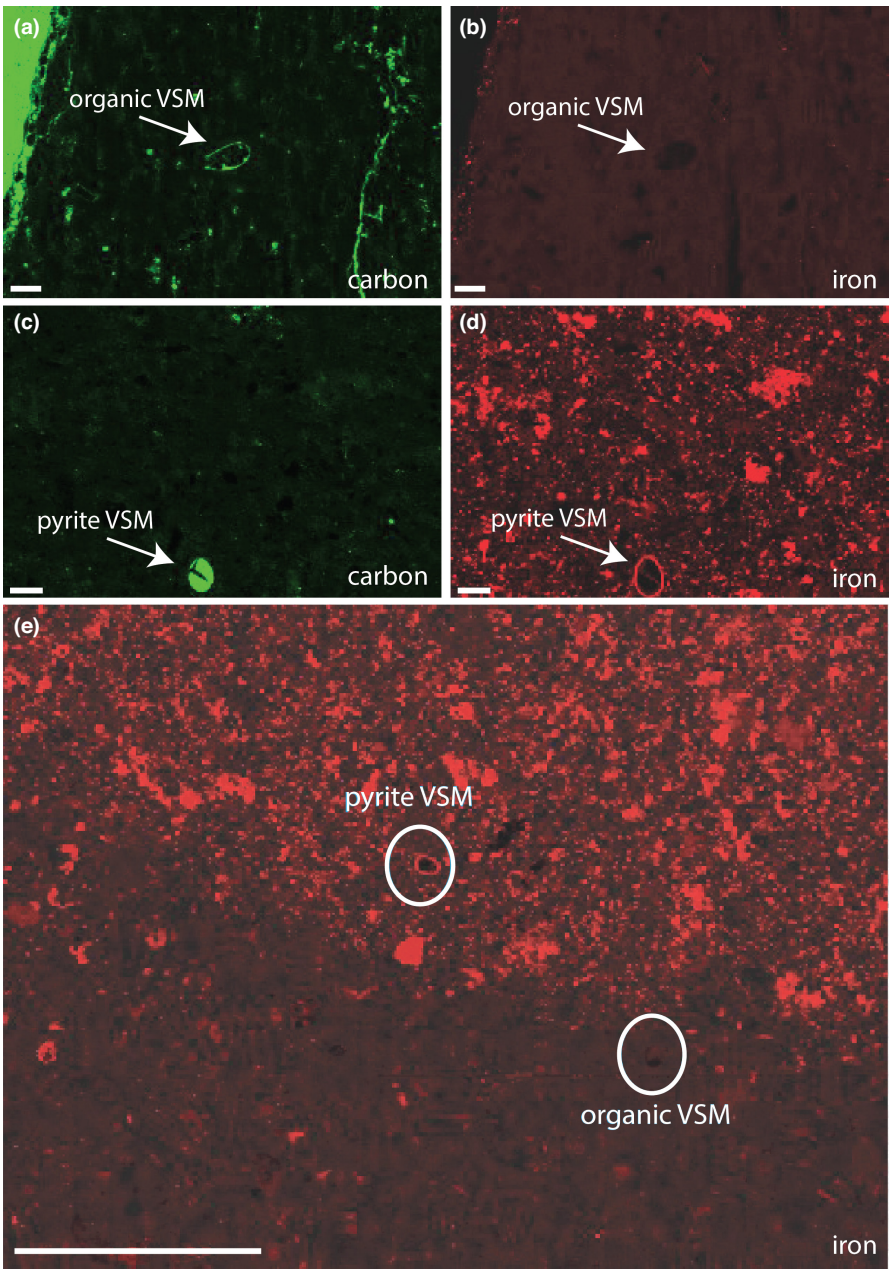

FIGURE 7 Wavelength dispersive spectroscopy elemental maps noting the spatial variation of carbon and iron concentrations within samples CS2 and CS3. Organic vase-shaped microfossils (VSMs) are associated with relatively iron-poor areas, and secondarily mineralized VSMs are associated with relatively iron-rich areas. (a) Carbon distribution in sample CS2; (CS2.1A). (b) Iron distribution within sample CS2, which is comparatively low; (CS2.1A). (c) Carbon distribution in sample CS3; (CS3.2). (d) Iron distribution within sample CS3, which is comparatively high: (CS3.2). (e) Composite of iron map and backscattered electron image to show the location of VSMs and iron distribution. Note the presence of an organic VSM within an Fe-poor (darker red) zone; (CS3.2). Scale bars are 50 μm in (a–d), and 500 μm in (e).

and as carbonaceous internal molds and suggested that this was the result of organic-rich material from the sedimentary environment infilling the tests. We hypothesize that the same process occurred in our samples, and thus herein refer to the internal carbonaceous material as exogenous carbonaceous material (ECM), and distinguish it from the wall carbonaceous material (WCM).

We interpret the ECM found in test interiors to be bitumen that was released from organic matter within Walcott shales. Bitumen is expelled from kerogen as kerogen is 'cracked' during catagenesis as temperature and pressure increases. The Walcott Member contains bituminous shales, is considered to have the highest source-rock potential of the Chuar Group, and is estimated to be in peak or late maturity for hydrocarbon production (Huntoon et al., 1999; Lillis, 2016; Summons et al., 1988). The occurrence of ECM within test interiors and partially attached and/or lining test walls (Figure 5f,j,g) suggests that ECM infiltrated and filled the entirety of the tests. Distinct crack-like patterns within the ECM suggest that after infiltration this material subsequently shrank and developed microfractures (Figure 5c–e,n), which may be a result of either compression (see test wall cracks pictured in Figure 5b,g,k) or an additional expulsion of hydrocarbons upon continued maturation after the initial infiltration of the test. If the latter interpretation is correct then the thin (~0.5 μm) dark form of ECM found within test wall cracks and coating test wall interiors and exteriors (Figure 5f,j) may represent these hydrocarbons. The Raman spectra of both the WCM and ECM are similar, suggesting either a similar chemical composition or comparable thermal maturity. EDS and sulfur speciation data suggest that ECM and WCM are chemically distinct (see following section for further discussion). Instead, we propose that likeness in Raman spectra is a result of similar thermal maturity, given that Summons et al. (1988)

14724669, 0, Downloaded from https://onlinelibrary.wiley.com/doi/10.1111/gbi.12544 by University Of California, Santa Barbara, Wiley Online Library on [01/03/2023]. See the Terms and Conditions (https://onlinelibrary.wiley.com/terms-and-conditions) on Wiley Online Library for rules of use; OA articles are governed by the applicable Creative Commons License

analyzed carbon isotopes and evaluated T-max values (an estimate of the stage of maturation) from kerogen and bitumen within the lower Walcott and concluded that both were syngenetic and indigenous to Chuar sediments.

Burial history models predict that the Kwagunt Formation entered the oil window in the Cretaceous and reached peak oil generation in the Oligocene (Huntoon et al., 1999; Lillis, 2016). If this is the source of the organic ECM within these specimens, how might bitumen have infiltrated VSM tests more than 600 million years after burial and lithification of the matrix? One possibility is that VSM tests were fluid filled, possibly with cell contents or porewater, at the time of deposition which prevented detrital filling. By example, Buijs et al. (2004) identified fluid (meteoric water, gas, and oil) within microborings in Pennsylvanian and Permian-aged brachiopods of Kansas, which are typically on the order of hundreds of microns in length and 1–10 μm in diameter. If test interiors were fluid-filled, bitumen could have permeated into test interiors and replaced this primary and/or secondary fluid. In this scenario, we might expect to find rare examples of VSMs in which the original fluid remains, but no such VSM was observed of the 66 total specimens. It is also possible that test cavities were mineralized during diagenesis and the quartz observed in test interiors in sample CS2 are partial or near complete internal molds. The ECM is more diffuse and 'web-like' in the interiors of VSMs from sample CS2 than CS3; we interpret this pattern to be a result of ECM flowing through microfractures within an internal mold. Alternatively, the ECM may represent organic-rich material that filled test interiors shortly after deposition. For example, VSMs from the Callison Lake Formation are filled with organic inclusions and are also found preserved as internal carbonaceous molds (Cohen et al., 2017; figures 4 and 7). This organic-rich material could then have expelled hydrocarbons as the Walcott sediments entered the oil window, which subsequently coated and flowed through test wall cracks (Figure 5f,j).

5.2 | Organic preservation and secondary mineralization of VSM test walls

Our results indicate that the Walcott shale VSMs are preserved with original organic walls, as fully mineral-replaced walls, or as a combination of original organic wall material with partial mineral replacement. We interpret the mineral distribution observed in sample CS3 to represent replacement and coating of carbonaceous walls by pyrite (Figures 5 and 6j–l, Figures S4 and S6). Pyrite can form as a result of microbial sulfate reduction (MSR), which oxidizes organic material while reducing sulfate to sulfide. Sulfides produced by MSR can react with Fe^{2+} and iron minerals to precipitate pyrite during early diagenesis ($Fe^{2+} + S^0 + HS^- \rightarrow FeS_2 + H^+$; Berg et al., 2020; Berner, 1970). Jarosite [$(K, Na, H_3O)Fe^{3+}{}_3(SO_4)_2(OH)_6$] found in association with pyritized VSMs may have formed from oxidation of pyrite (Zolotov & Shock, 2005). Thus, pyrite was likely the primary mineral that replaced test walls, and jarosite formed secondarily from pyrite during oxidative conditions.

While the pyrite and jarosite are secondary minerals formed during diagenesis, the carbonaceous material of the wall appears to be primary. This is consistent with the occurrence of pyrite in partially pyritized specimens (Figure 5b,d,j,l), which suggests pyrite nucleation followed the decay of the organic wall from both the exterior and interior of the test. Furthermore, it seems clear for several reasons that the organic walls are distinct from the ECM, and not simply the result of ECM infiltrating an originally mineralized test or a void created by the decay of an original organic test (cf. Rasmussen & Muhling, 2019; Rasmussen et al., 2021). First, several specimens show evidence for ECM cross-cutting test walls, suggesting that the organic wall material is primary, and the ECM was secondarily emplaced (Figure 5g,j). Second, the ECM and WCM appear strikingly different in transmitted light microscopy (translucent walls and opaque ECM, e.g., Figure 3j). Third, the presence of FeS and increased contributions of sulfonate and structural sulfates distinguishes the composition of the organic wall material from the ECM (Figure 9b). Finally, there is little evidence for silicon or calcium in test walls, as might be expected if the organic walls of the VSMs reflect secondary filling of mineralized casts (or an original mineralized test) by bitumen (Rasmussen et al., 2021; Rasmussen & Muhling, 2019) (Figure 6, Figure S5). Based on this evidence, we propose that the carbonaceous test walls are mature organic material that reflects the original test wall and are distinct from the ECM.

5.3 | Controls on organic preservation of VSMS

The original organic material of which VSMs were composed is not refractory in the same way as that of most Proterozoic organic-walled microfossils. VSMs are commonly preserved as casts and molds in a wide variety of mineral types, sometimes co-occurring in fossil assemblages with unmineralized organic-walled microfossils. This may suggest that original VSM wall composition is more reactive, i.e., is composed of less intrinsically recalcitrant organic materials, and is therefore prone to replacement (Riedman et al., 2018). VSMs have only been confirmed preserved with organic walls by Cohen et al. (2017) and Morais et al. (2017) and in this study (it should be noted that this could be a reflection that some VSM-bearing assemblages like the Chuar Group have been more extensively studied than others). Why are VSMs preserved organically in shales of the Chuar Group? One hypothesis is that the Chuar shale VSMs were physically protected from biological degradation. An alternative possibility is that VSM test material was chemically transformed into a more stable form.

Mineral barriers can prevent decay and promote organic preservation, such as the development of early carbonate cements (Gaines et al., 2012; Morais et al., 2017) or clay mineral coatings around fossil material (Anderson et al., 2018, 2020, 2021; Gabbott, 1998; Orr et al., 1998; Wacey et al., 2014). However, we found no obvious evidence for protective coatings of carbonate or clay minerals that may have promoted organic preservation in our study. Aluminum-rich clay minerals are observed in test interiors of all observed ($n = 46$) sample

14724669, 0, Downloaded from https://onlinelibrary.wiley.com/doi/10.1111/gbi.12544 by University Of California, Santa Barbara, Wiley Online Library on [01/03/2023]. See the Terms and Conditions (https://onlinelibrary.wiley.com/terms-and-conditions) on Wiley Online Library for rules of use; OA articles are governed by the applicable Creative Commons License

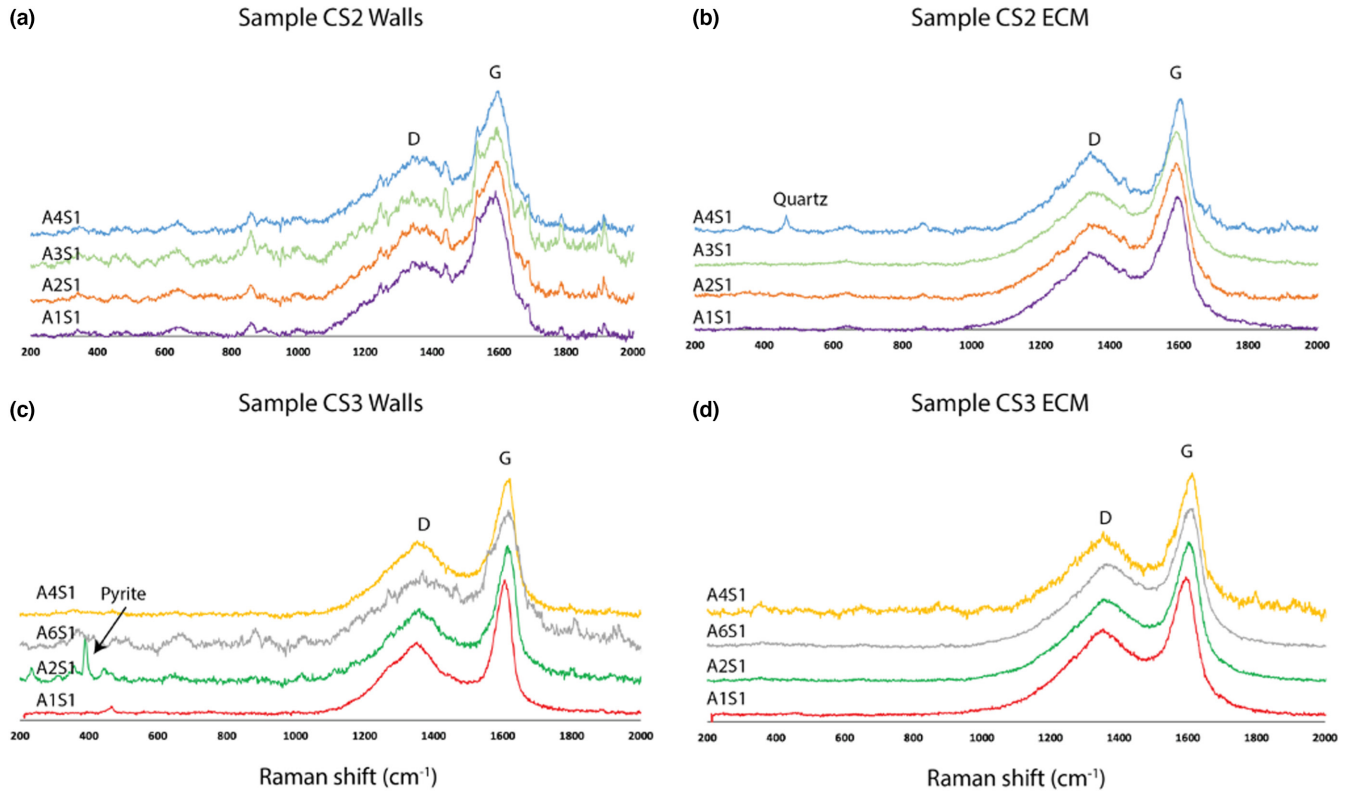

FIGURE 8 Baseline subtracted Raman spectra of test walls and exogenous carbonaceous material (ECM). The spectra of vase-shaped microfossil test walls and ECM materials are similar, which may imply similar chemical compositionor thermal maturity. (a) Raman spectra of walls in sample CS2, pictured in Figure 4. A1S1 is Figure 4h, A2S1 is Figure 4f, A3S1 is Figure 4g, A4S1 is Figure 4e. (b) Raman spectra of ECM in sample CS2, pictured in Figure 4. (c) Raman spectra of walls in sample CS3, pictured in Figures 4 and 5. A1S1 is Figure 4i, A2S1 is Figure 5n, A4S1 is Figure 5k, A6S1 is Figure 8p. (d) Raman spectra of ECM in sample CS2, pictured in Figures 4 and 5.

CS3 VSMs. Cohen et al. (2017) reported a similar but rare preservation mode in VSMs from the Callison Lake Formation, where VSM test interiors were infilled with Al-rich clay minerals. The clay minerals observed in sample CS3 VSMs, however, infill the microfractures and voids created by the shrunken bitumen (Figures 4j,l,o and 5a) which suggests that these minerals formed post hydrocarbon infiltration, possibly by precipitation from pore fluids or adsorption of detrital particles (Liu et al., 2004). The clay minerals observed would not be relevant to organic preservation if ECM infilled VSM test interiors in the Cretaceous or later (Huntoon et al., 1999; Lillis, 2016), but may be relevant if ECM filled test interiors shortly after deposition. However, sample CS2 VSMs, all of which are organically preserved, are filled with siliceous internal molds (which may reflect differing chemistries between the pore fluids of both samples) and show no such association with clay minerals. Thus it is unclear what role, if any, clay minerals may have played in the organic preservation of Chuar VSMs.

Labile organic matter can be transformed into more stable forms through chemical processes such as abiotic sulfurization, and we speculate that sulfurization may have played a role in preserving organic VSMs. During sulfurization in sediments or in the water column, reduced sulfur is incorporated into organic remains by reacting with functional groups within organic compounds. This transformation causes organic material to be less available for degradation, thus aiding in organic preservation (Brassell et al., 1986; Raven et al., 2021; Sinninghe Damsté & De Leeuw, 1987, 1990; Werne et al., 2008). Sulfurization may have played an important role in the preservation of large quantities of organic matter during Cretaceous anoxia events (Raven et al., 2018, 2021) and has influenced the preservation of organic fossil material, including bone marrow, melanin, biomarkers, and invertebrate chitinous tissue (McNamara et al., 2006; Melendez et al., 2013; McNamara et al., 2016; Olcott et al., 2022). Three conditions required for sulfurization to occur are: (1) a reduced sulfur source such as bisulfide (HS^-) or polysulfides (S_x^{2-}), (2) the presence of functionalized (i.e., labile) organic matter, and (3) limited availability of reactive iron (Werne et al., 2004). All of these paleoenvironmental conditions were met during the preservation of organic VSMs. First, Walcott shales are sulfide-rich (Johnston et al., 2010) and sulfur is associated with organic test walls (Figure 6, Figures S2 and S5). Second, we argue that VSM organic material is not recalcitrant given both (a) the rarity of occurrences of organic preservation and (b) the variety of ways in which they are preserved, which is consistent with an easily degradable composition. Finally, if Walcott shales were deposited in a euxinic, high TOC environment, sulfide production via MSR would have removed ferrous iron from the environment through the formation of pyrite (Johnston et al., 2010),

14724669, 0, Downloaded from https://onlinelibrary.wiley.com/doi/10.1111/gbi.12544 by University Of California, Santa Barbara, Wiley Online Library on [01/03/2023]. See the Terms and Conditions (https://onlinelibrary.wiley.com/terms-and-conditions) on Wiley Online Library for rules of use; OA articles are governed by the applicable Creative Commons License

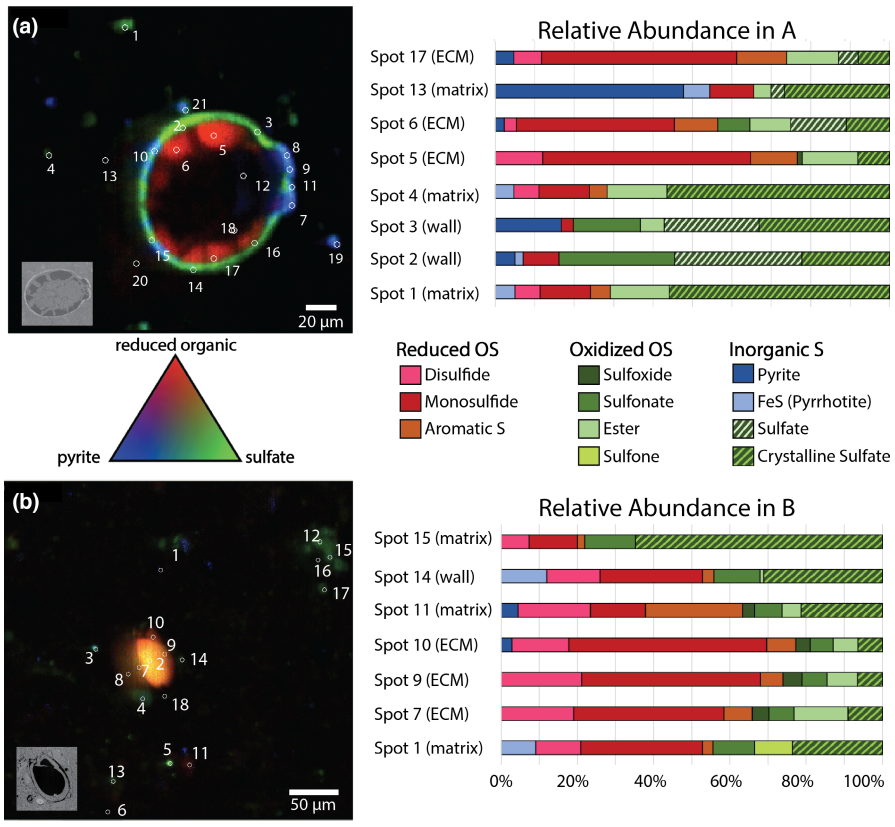

FIGURE 9 Sulfur speciation of vase-shaped microfossil and matrix material from sample CS3 by X-ray absorption spectroscopy (XAS) and X-ray fluorescence. Reduced organic sulfur is found within organically preserved test walls and exogenous carbonaceous material, suggesting sulfurization likely occurred during diagenesis. Left, tricolor XANES fits to multi-energy maps (with backscattered electron images inset) showing reduced organic sulfur (red), sulfate (green) and pyrite (blue), with 1 µm map step size. Relative abundance from fitted XAS spectra of numbered spots in map A are shown in top right, and in map B in bottom right (see Figures S12 and S13 for complete spectra).

and indeed we see low iron concentrations associated with organic VSMs (Figure 7).

Immediate products of organic matter sulfurization are primarily organic monosulfides and disulfides, both of which can mature into aromatic structures during diagenesis (Amrani & Aizenshtat, 2004; Gelin et al., 1998). Therefore, if sulfurization occurred, we would expect to see evidence of reduced organic sulfur species within the VSMs and organic material of the matrix. Reduced organic sulfur species are indeed present at low concentrations throughout the matrix, and they are highly concentrated within the ECM. XAS spectra for ECM consistently comprise ~70% reduced organic S and available ECM spectra for specimens in Figure 9 average 47% organic monosulfides, 13% organic disulfides, and 9% aromatics. The remaining sulfur in ECM includes varying amounts of inorganic sulfate and oxidized organic S (averaging 7% sulfonate and 11% sulfate ester). Bitumen and other crude oil products are often enriched in reduced organic sulfur as a result of sulfurization in early diagenesis (Sinninghe Damsté & De Leeuw, 1990). Given that the thermal maturity history of ECM and WCM are similar (see Section 4.4 above), it is probable that ECM formed from organic matter within Walcott Shales, suggesting that sulfurization processes occurred in the same environment as the VSMs.

Oxidized organic sulfur species were additionally identified within partially mineralized VSM test walls where they represent ~29% and ~18% of total S (Figure 9a, spots 2 and 3). The remaining sulfur in these regions consists of structural sulfates (~50%) (e.g. gypsum or jarosite), reduced organic S (≤10%) and iron monosulfides (≤15%). Inorganic sulfates are likely the products of pyrite oxidation. Conversely, oxidized organic sulfur compounds are common in primary organic material (i.e., sulfonolipids in cell walls) and may therefore represent remnant primary sulfur from the VSM organism (Canfield, 2001). Alternatively, it is possible that sulfonates in VSM test walls are a direct result of oxidation of organic sulfides originally produced via abiotic sulfurization. Microbial sulfate reduction significantly fractionates $\delta^{34}S$ compared to seawater sulfate, so organic sulfur formed via MSR-generated sulfides should be depleted in $\delta^{34}S$, whereas biotic sulfur would closely match environmental sulfate $\delta^{34}S$ compositions (Canfield et al., 2010; Kaplan & Rittenberg, 1964). Future investigations could compare $\delta^{34}S$ isotope fractionation between extractable bitumens, which are rich in reduced organic sulfur and therefore likely sulfurized, and isolated VSM wall materials to determine whether the organic sulfur observed in the VSMs is primary or secondary.

We observed a preservational gradient between complete organic preservation and complete mineralization (Figure 10a). Schiffbauer et al. (2014) observed a similar taphonomic gradient in the macrofossil *Conotubus* and proposed a model in which sedimentation rate variation, which influences the time that a decaying organism spends in the MSR zone and undergoes MSR-mediated pyritization, promotes such a gradient. However, this is unlikely to apply here because of the compositional and size differences between *Conotubus* and VSMs. The time scale over which the organic matter of an individual organic (possibly proteinaceous, see below for further discussion) microfossil would degrade and subsequently mineralize is likely shorter than that of a macroscopic organic tube. Recent studies confirm that pyrite can form in weeks to months

14724669, 0, Downloaded from https://onlinelibrary.wiley.com/doi/10.1111/gbi.12544 by University Of California, Santa Barbara, Wiley Online Library on [01/03/2023]. See the Terms and Conditions (https://onlinelibrary.wiley.com/terms-and-conditions) on Wiley Online Library for rules of use; OA articles are governed by the applicable Creative Commons License

under sulfidic conditions when facilitated by sulfate-reducing microbial activity (Berg et al., 2020; Duverger et al., 2020), which is probably faster than VSMs would be buried by sediment and moved into the MSR zone. Therefore, differences in MSR zone residence time are not sufficient to explain the variation in preservation modes observed here.

Instead, based on EPMA and XAS data in this study (see Figure 7e and matrix relative abundance in Figure 9) illustrating spatial (mm scale or smaller) differences within the shale matrix of these samples, we suggest that preservation was primarily controlled by variation in the ratio of iron to functionalized organic matter (i.e., labile VSM test material) (Figure 10b). In this model, when reduced sulfur is present and iron is absent (or in low concentrations), organic walls are sulfurized. Under intermediate concentrations of iron relative to functionalized organic matter, some organic wall material becomes sulfurized while a portion is replaced by pyrite. High iron concentrations result in complete replacement of organic wall material by pyrite. If true, our model suggests that organic VSMs and other microfossils that are more labile than typical organic-walled microfossils, may be targeted within iron-poor horizons of black, sulfide-rich shales. We propose that the key factors resulting in original organic wall preservation are the presence of reduced sulfur and low concentrations of iron relative to reactive organic material, both of which occurred, at least intermittently, in shales of the lower Walcott Member.

Based on our model, we suggest that organic VSM preservation requires different conditions than organic-walled microfossil (OWM) preservation. OWMs are typically poorly preserved or absent in TOC-rich shales showing evidence of deposition under euxinic water columns (Nagy et al., 2009; Woltz et al., 2021). In addition, VSMs are rarely preserved organically, whereas organic preservation of OWMs in shales is ubiquitous. Furthermore, their appearance under transmitted light (clear vs. brown) suggests very different styles of organic preservation. With this considered, different target rock types (high vs. low TOC) may be necessary in Proterozoic microfossil studies.

5.4 | Comparison with other Neoproterozoic VSMS reported globally

Our observations suggest that organic VSMs are more widespread globally than currently recognized. The organic VSM tests observed here are primarily colorless and appear translucent in transmitted light microscopy; they could easily be mistaken for siliceous casts, as we believe may have been the case with VSMs from this same stratigraphic horizon reported by Porter and Knoll (2000; figure 1B).

Furthermore, the conditions that promoted the preservation of organic VSMs in the Walcott shales were also present in coeval

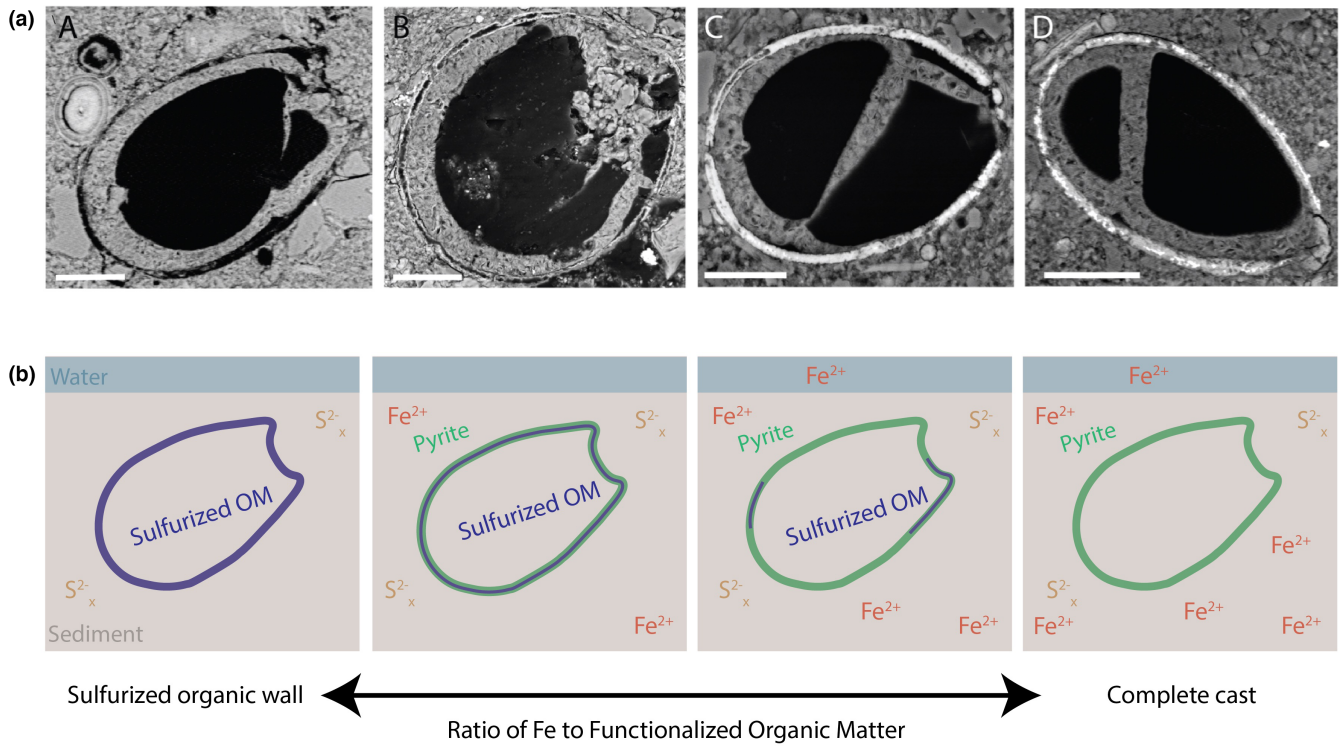

FIGURE 10 Taphonomic gradient and proposed model of preservation. (a) Backscattered electron images illustrating continuum in preservation modes of vase-shaped microfossils from sample CS3. Scale bar = 25 μm. (b) Proposed model of preservation, dependent on the ratio of iron to functionalized (i.e., reactive) organic matter (OM). Sulfurized organic material is shown in green and pyrite-replaced walls are shown in navy. The top blue area represents seawater and the gray area represents sediment. When the ratio of iron to functionalized organic matter is low, sulfurization of organic test material is extensive and organic preservation is observed. When the ratio is high, complete mineralization is observed.

14724669, 0, Downloaded from https://onlinelibrary.wiley.com/doi/10.1111/gbi.12544 by University Of California, Santa Barbara, Wiley Online Library on [01/03/2023]. See the Terms and Conditions (https://onlinelibrary.wiley.com/terms-and-conditions) on Wiley Online Library for rules of use; OA articles are governed by the applicable Creative Commons License

environments, so it is possible that elsewhere, VSMs are similarly preserved. Horodyski (1993) reported carbonaceous VSMs extracted from shales of the upper Awatubi Member of the Chuar Group. Given the similarity in lithologies (organic- and pyrite-rich shales), it is possible that sulfurization also enabled the organic preservation of Awatubi VSMs. Riedman et al. (2018) described possible organically-preserved VSMs in shales of the Togari Group, Tasmania, that co-occur with VSM internal molds of framboidal pyrite. Perhaps this reflects intermittent changes in reactive iron availability in anoxic and sulfide rich waters, resulting in an environment that promoted the sulfurization of organic matter as well.

In addition, there is evidence that additional pathways, in carbonates and perhaps in cherts, may be capable of preserving organic VSM tests. Morais et al. (2017) reported organically-preserved VSMs encased in early diagenetic carbonate cement, which they concluded were vital in organic preservation. It is possible that early cementation was integral in other reports of carbonaceous VSMs found within carbonates. For example, Riedman et al. (2018) reported organic VSMs from oolites and pisolites of the Upper Limestone-Dolomite Series of the Eleonore Bay Group, Greenland. Knoll et al. (1991; figure 7.1) illustrated a VSM they describe as organically-preserved from silicified carbonates of the Draken Conglomerate Formation, Svalbard, and although no EDS or other elemental data are included in the report, this may represent yet another pathway. Finally, Knoll and Calder (1983) reported carbonaceous VSMs from both pyritic black shales and silicified carbonates of the Ryssö Formation, Svalbard, highlighting that the special conditions necessary for organic preservation could be met in multiple environments within an assemblage.

5.5 | Test composition and implications

While only rare occurrences of eukaryotic biomineralization in the Proterozoic are reported (Cohen & Knoll, 2012), workers have suggested that some VSMs may have had a mineralized composition in life. Porter et al. (2003) identified *Melicerion poikilon* within the Chuar Group and hypothesized that its honeycomb-like test wall reflects an organic test in which mineralized scales were embedded and suggested that it may be similar to *Caraburina granosa* Kraskov, 1989, a species of VSM from Tien Shan, Kyrgyzstan, that was interpreted to be covered with regularly arranged, raised, circular structures. However, Riedman et al. (2018) demonstrated that the Tien Shan specimens were not tests composed of scales but rather represent internal molds of amalgamated pyrite framboids, similar to those found in the Togari Group of Tasmania (Riedman et al., 2018: figures 5.1–5.3) and the Ryssøya Member, Elbobreen Formation of Svalbard (Martí Mus et al., 2020; figure 6a). Morais et al. (2017) found siliceous-walled *Cycliocyrillium simplex*, *C. torquata*, and *Taruma rata* in the Urucum Formation, Brazil, and described how secondary silicification could not account for the composition of these fossils because the early diagenetic carbonate cement coating interiors and exteriors of the tests was not disrupted by silica-replacement. Instead, they argue that these species possessed mineralized tests in life. Although we were unable to identify *C. simplex* or *T. rata* in the samples studied here (in fact, the latter has not been identified in the Chuar Group; Morais et al., 2019), evidence for silica was lacking within test walls of *C. torquata* (Figures 4e,i and 5k) found in our Chuar samples. This may suggest that the Urucum Formation VSMs were secondarily silicified without disrupting the surrounding early diagenetic cement. Alternatively, the differences between the Chuar and Urucum VSMs reflects intraspecific variation as single species of modern testate amoebae who construct their tests through agglutination can build organic tests if deprived of mineral particles (Ogden, 1988). Moreover, it is additionally plausible that the siliceous-walled VSMs identified as *C. torquata* belong to a distinct, morphologically similar, but compositionally different species. For example, within the euglyphid testate amoebae (a primarily siliceous group which molecular clock data suggests to have originated before the Carboniferous), closely related *Paulinella* and *Ovulinata* build siliceous and organic tests, respectively (Howe et al., 2011; Lahr et al., 2015, 2019). Finally, Riedman et al. (2021) found evidence for biomineralized phosphatic scales co-occurring with VSMs from several assemblages and suggested these might be part of a VSM test, though a definitive association with VSM tests was not demonstrated.

The organic portions of modern arcellinid tests are made from protein (Ogden, 1984). Given that VSMs are thought to represent early arcellinids (Lahr et al., 2019; Porter & Riedman, 2019), assuming that Tonian VSMs were also proteinaceous or part proteinaceous in life is a reasonable hypothesis. Proteins display low preservation potential when compared to molecules such as complex carbohydrates and lipids. Nevertheless, researchers detect proteins preserved in Mesozoic and even Paleozoic fossil animals (Briggs & Summons, 2014; Cody et al., 2011; Lee et al., 2017; Myers et al., 2018; Wiemann et al., 2020). Furthermore, McNamara et al. (2016) found sulfurized melanin within Late Miocene frog tissue. If VSMs are proteinaceous (though likely sulfurized and heavily modified by diagenesis), it would extend the fossil record of preserved original proteinaceous material into the Neoproterozoic.

6 | CONCLUSION

VSMs from black shales of the lower Walcott Member of the Chuar Group, Grand Canyon, Arizona are preserved as original organic tests and as partial and complete casts composed of pyrite and jarosite. Pyrite replaced, and sometimes coated, primary organic test material, with jarosite forming later via the oxidation of pyrite. All VSMs internal cavities are infilled with an exogenous carbon-rich material. This material may have either entered tests shortly after deposition, or at some point in the Cretaceous or later as the Walcott Member entered the oil window, replacing any fluid that may have been preserved within sample CS3 VSMs, or infiltrating internal molds within sample CS2 VSMs. We suggest that sulfide abundance, organic-rich sediments, and low concentrations of available

14724669, 0, Downloaded from https://onlinelibrary.wiley.com/doi/10.1111/gbi.12544 by University Of California, Santa Barbara, Wiley Online Library on [01/03/2023]. See the Terms and Conditions (https://onlinelibrary.wiley.com/terms-and-conditions) on Wiley Online Library for rules of use; OA articles are governed by the applicable Creative Commons License

iron facilitated sulfurization of organic test material, thus promoting organic preservation. We further propose that the extent of organic test preservation may be controlled by variations in the ratio of iron to reactive organic matter within the environment, with fully pyritized tests resulting from high ratios of iron to reactive organic matter. Organic VSMs are rarely reported, but in fact, may be more globally widespread and simply overlooked, given that organic walls appear similar to mineralized walls under transmitted light.

ACKNOWLEDGEMENTS

Samples were collected from unceded lands of the Kaibab tribe of the Southern Paiute people. We thank Lee Sharpnack for assistance with sample preparation and Gareth Seward for assistance with SEM/EPMA analysis, data presentation, and for helpful discussion. We thank Simon Darroch, Leigh Anne Riedman and Bruce Tiffney for providing valuable comments on an earlier version of this manuscript. The authors thank the editor and three anonymous reviewers for constructive criticism that improved the quality of this manuscript. Tingle acknowledges funding from the Department of Earth Science and Interdepartmental Graduate Program in Marine Science at University of California, Santa Barbara (UCSB) and from the Clay Minerals Society. Porter acknowledges funding from the National Science Foundation Grant/Award Number: EAR-1855092. Czaja acknowledges funding from NASA and the National Science Foundation Grant/Award Number: EAR-2029521. Use of the Stanford Synchrotron Radiation Lightsource, SLAC National Accelerator Laboratory, is supported by the U.S. Department of Energy, Office of Science, Office of Basic Energy Sciences under Contract No. DE-AC02-76SF00515. The SSRL Structural Molecular Biology Program is supported by the DOE Office of Biological and Environmental Research, and by the National Institutes of Health, National Institute of General Medical Sciences (P30GM133894). The contents of this publication are solely the responsibility of the authors and do not necessarily represent the official views of NIGMS or NIH.

FUNDING INFORMATION

University of California, Santa Barbara, Department of Earth Science and Interdepartmental Graduate Program in Marine Science; Clay Minerals Society; National Science Foundation Grant/Award Number: EAR-1855092; National Science Foundation Grant/Award Number: EAR-2029521. U.S. Department of Energy contract no. DE-AC02-76SF00515; National Institutes of Health, National Institutes of General Medical Sciences (P30GM133894).

CONFLICT OF INTEREST

The authors declare no competing interests.

DATA AVAILABILITY STATEMENT

The data that support the findings of this study are available within this report, its supplementary material, and from the corresponding author upon request. Thin sections of original material may be made available to study by contacting K.E.T. or S.M.P.

ORCID

Kelly E. Tingle https://orcid.org/0000-0002-6121-9677
Susannah M. Porter https://orcid.org/0000-0002-4707-9428

REFERENCES

Amrani, A., & Aizenshtat, Z. (2004). Reaction of polysulfide anions with α, β unsaturated isoprenoid aldehydes in aquatic media: Simulation of oceanic conditions. *Organic Geochemistry*, *35*, 909–921. https://doi.org/10.1016/j.orggeochem.2004.04.002

Anderson, R. P., Tosca, N. J., Cinque, G., Frogley, M. D., Lekkas, I., Akey, A., Hughes, G. M., Bergmann, K. D., Knoll, A. H., & Briggs, D. E. (2020). Aluminosilicate haloes preserve complex life approximately 800 million years ago. *Interface Focus*, *10*(4), 20200011. https://doi.org/10.1098/rsfs.2020.0011

Anderson, R. P., Tosca, N. J., Gaines, R. R., Koch, N. M., & Briggs, D. E. (2018). A mineralogical signature for Burgess Shale–type fossilization. *Geology*, *46*(4), 347–350. https://doi.org/10.1130/G39941.1

Anderson, R. P., Tosca, N. J., Saupe, E. E., Wade, J., & Briggs, D. E. (2021). Early formation and taphonomic significance of kaolinite associated with burgess shale fossils. *Geology*, *494*, 355–359. https://doi.org/10.1130/G39941.1

Berg, J. S., Duverger, A., Cordier, L., Laberty-Robert, C., Guyot, F., & Miot, J. (2020). Rapid pyritization in the presence of a sulfur/sulfate-reducing bacterial consortium. *Scientific Reports*, *10*(1), 1–13. https://doi.org/10.1038/s41598-020-64990-6

Berner, R. A. (1970). Sedimentary pyrite formation. *American Journal of Science*, *268*(1), 1–23. https://doi.org/10.2475/ajs.268.1.1

Berner, R. A., & Raiswell, R. (1983). Burial of organic carbon and pyrite sulfur in sediments over phanerozoic time: A new theory. *Geochimica et Cosmochimica Acta*, *47*(5), 855–862.

Berney, C., & Pawlowski, J. (2006). A molecular time-scale for eukaryote evolution recalibrated with the continuous microfossil record. *Proceedings of the Royal Society B: Biological Sciences*, *273*(1596), 1867–1872. https://doi.org/10.1098/rspb.2006.3537

Binda, P., & Bokhari, M. M. (1980). Chitinozoan-like microfossils in a late Precambrian dolostone from Saudi Arabia. *Geology*, *8*, 70–71. https://doi.org/10.1130/0091-7613(1980)8%3C70:CMIALP%3E2.0.CO;2

Bloeser, B. (1985). *Melanocyrillium*, a new genus of structurally complex late Proterozoic microfossils from the Kwagunt Formation (Chuar Group), Grand Canyon, Arizona. *Journal of Paleontology*, *59*, 741–765.

Bloeser, B., Schopf, J. W., Horodyski, R. J., & Breed, W. J. (1977). Chitinozoans from the late Precambrian Chuar Group of the Grand Canyon, Arizona. *Science*, *195*(4279), 676–679. https://doi.org/10.1126/science.195.4279.676

Brassell, S. C., Lewis, C. A., De Leeuw, J. W., De Lange, F., & Sinninghe Damsté, J. S. (1986). Isoprenoid thiophenes: Novel products of sediment diagenesis? *Nature*, *320*(6058), 160–162. https://doi.org/10.1038/320160a0

Briggs, D. E., & Summons, R. E. (2014). Ancient biomolecules: Their origins, fossilization, and role in revealing the history of life. *BioEssays*, *36*(5), 482–490. https://doi.org/10.1002/bies.201400010

Brocks, J. J., Jarrett, A. J. M., Sirantoine, E., Kenig, F., Moczydłowska, M., Porter, S. M., & Hope, J. (2016). Early sponges and toxic protists: Possible sources of cryostane, an age diagnostic biomarker antedating Sturtian Snowball Earth. *Geobiology*, *14*(2), 129–149. https://doi.org/10.1111/gbi.12165

Buijs, G. J., Goldstein, R. H., Hasiotis, S. T., & Roberts, J. A. (2004). Preservation of microborings as fluid inclusions. *The Canadian Mineralogist*, *42*(5), 1563–1581. https://doi.org/10.2113/gscanmin.42.5.1563

Canfield, D. E. (2001). Biogeochemistry of sulfur isotopes. *Reviews in Mineralogy and Geochemistry*, *43*, 607–636. https://doi.org/10.2138/gsrmg.43.1.607

14724669, 0, Downloaded from https://onlinelibrary.wiley.com/doi/10.1111/gbi.12544 by University Of California, Santa Barbara, Wiley Online Library on [01/03/2023]. See the Terms and Conditions (https://onlinelibrary.wiley.com/terms-and-conditions) on Wiley Online Library for rules of use; OA articles are governed by the applicable Creative Commons License

Canfield, D. E., Farquhar, J., & Zerkle, A. L. (2010). High isotope fractionations during sulfate reduction in a low-sulfate euxinic ocean analog. *Geology*, *38*, 415–418. https://doi.org/10.1130/G30723.1

Carlisle, E. M., Jobbins, M., Pankhania, V., Cunningham, J. A., & Donoghue, P. C. (2021). Experimental taphonomy of organelles and the fossil record of early eukaryote evolution. *Science Advances*, *7*(5), eabe9487. https://doi.org/10.1126/sciadv.abe9487

Cody, G. D., Gupta, N. S., Briggs, D. E., Kilcoyne, A. L. D., Summons, R. E., Kenig, F., Plotnick, R. E., & Scott, A. C. (2011). Molecular signature of chitin-protein complex in Paleozoic arthropods. *Geology*, *39*(3), 255–258. https://doi.org/10.1130/G31648.1

Cohen, P. A., Irvine, S. W., & Strauss, J. V. (2017). Vase-shaped microfossils from the Tonian Callison Lake formation of Yukon, Canada: Taxonomy, taphonomy and stratigraphic palaeobiology. *Palaeontology*, *60*(5), 683–701. https://doi.org/10.1111/pala.12315

Cohen, P. A., & Knoll, A. H. (2012). Scale microfossils from the mid-neoproterozoic Fifteenmile Group, Yukon territory. *Journal of Paleontology*, *86*(5), 775–800. https://doi.org/10.1666/11-138.1

Dehler, C. M., Elrick, M., Karlstrom, K. E., Smith, G. A., Crossey, L. J., & Timmons, J. M. (2001). Neoproterozoic Chuar Group (~800–742 ma), Grand Canyon: A record of cyclic marine deposition during global cooling and supercontinent rifting. *Sedimentary Geology*, *141*, 465–499. https://doi.org/10.1016/S0037-0738(01)00087-2

Dehler, C. M., Gehrels, G., Porter, S. M., Heizler, M., Karlstrom, K. E., Cox, G., Crossey, L. J., & Timmons, J. M. (2017). Synthesis of the 780–740 ma Chuar, Uinta Mountain, and Pahrump (ChUMP) groups, western USA: Implications for Laurentia-wide cratonic marine basins. *Geological Society of America Bulletin*, *129*, 607–624. https://doi.org/10.1130/B31532.1

Duverger, A., Berg, J. S., Busigny, V., Guyot, F., Bernard, S., & Miot, J. (2020). Mechanisms of pyrite formation promoted by sulfate-reducing bacteria in pure culture. *Frontiers in Earth Science*, *8*, 588310. https://doi.org/10.3389/feart.2020.588310

Eyster, A., Weiss, B. P., Karlstrom, K., & Macdonald, F. A. (2020). Paleomagnetism of the Chuar Group and evaluation of the late Tonian Laurentian apparent polar wander path with implications for the makeup and breakup of Rodinia. *Geological Society of America Bulletin*, *132*(3–4), 710–738.

Fairchild, T. R., Barbour, A. P., & Haralyi, N. L. (1978). Microfossils in the "Eopaleozoic" Jacadigo Group at Urucum, Mato Grosso, Southwest Brazil. *Boletim IG (Universidade de Sao Paulo, Instituto de Geociencias)*, *9*, 74–79.

Ford, T. D., & Breed, W. J. (1973). Late Precambrian Chuar Group, Grand Canyon, Arizona. *Geological Society of America Bulletin*, *84*, 1243–1260. https://doi.org/10.1130/0016-7606(1973)84<1243:LPCGGC>2.0.CO;2

Gabbott, S. E. (1998). Taphonomy of the Ordovician Soom Shale Lagerstätte: An example of soft tissue preservation in clay minerals. *Palaeontology*, *41*, 631–668.

Gaines, R. R., Hammarlund, E. U., Hou, X., Qi, C., Gabbott, S. E., Zhao, Y., Peng, J., & Canfield, D. E. (2012). Mechanism for burgess shale-type preservation. *Proceedings of the National Academy of Sciences*, *109*(14), 5180–5184.

Gelin, F., Kok, M. D., de Leeuw, J. W., & Damsté, J. S. S. (1998). Laboratory sulfurisation of the marine microalga *Nannochloropsis salina*. *Organic Geochemistry*, *29*, 1837–1848. https://doi.org/10.1016/S0146-6380(98)00171-5

Green, J. W., Knoll, A. H., & Swett, K. (1988). Microfossils from oolites and pisolites of the upper Proterozoic Eleonore Bay Group, central East Greenland. *Journal of Paleontology*, *62*(6), 835–852.

Horodyski, R. J. (1993). Paleontology of Proterozoic shales and mudstones: Examples for the Belt Supergroup, Chuar Group and Pahrump Group, western USA. *Precambrian Resesarch*, *61*, 241–278. https://doi.org/10.1016/0301-9268(93)90116-J

Horodyski, R. J., & Bloeser, B. (1983). Possible eukaryotic algal filaments from the late Proterozoic Chuar Group, Grand Canyon, Arizona. *Journal of Paleontology*, *57*, 321–326.

Howe, A. T., Bass, D., Scoble, J. M., Lewis, R., Vickerman, K., Arndt, H., & Cavalier-Smith, T. (2011). Novel cultured protists identify deep-branching environmental DNA clades of Cercozoa: New genera *Tremula*, *Micrometopion*, *Minimassisteria*, *Nudifila*, *Peregrinia*. *Protist*, *162*, 332–372. https://doi.org/10.1016/j.protis.2010.10.002

Huntoon, J. E., Hansley, P. L., & Naeser, N. D. (1999). The search for a source rock for the giant tar sand triangle accumulation, southeastern Utah. *American Association of Petroleum Geologists Bulletin*, *83*(3), 467–495.

Johnston, D. T., Poulton, S. W., Dehler, C., Porter, S., Husson, J., Canfield, D. E., & Knoll, A. H. (2010). An emerging picture of Neoproterozoic ocean chemistry: Insights from the Chuar Group, Grand Canyon, USA. *Earth and Planetary Science Letters*, *290*, 64–73. https://doi.org/10.1016/j.epsl.2009.11.059

Kaplan, I. R., & Rittenberg, S. C. (1964). Microbiological fractionation of sulphur isotopes. *Microbiology*, *34*, 195–212. https://doi.org/10.1099/00221287-34-2-195

Karlstrom, K., Hagadorn, J., Gehrels, G., Matthews, W., Schmitz, M., Madronich, L., Mulder, J., Pecha, M., Giesler, D., & Crossey, L. (2018). Cambrian Sauk transgression in the Grand Canyon region redefined by detrital zircons. *Nature Geoscience*, *11*, 438–443. https://doi.org/10.1038/s41561-018-0131-7

Karlstrom, K. E., Bowring, S. A., Dehler, C. M., Knoll, A. H., Porter, S. M., Marais, D. J. D., Weil, A. B., Sharp, Z. D., Geissman, J. W., Elrick, M. B., & Timmons, J. M. (2000). Chuar Group of the Grand Canyon: Record of breakup of Rodinia, associated change in the global carbon cycle, and ecosystem expansion by 740 Ma. *Geology*, *28*(7), 619–622. https://doi.org/10.1130/0091-7613(2000)28%3C619:CGOTGC%3E2.0.CO;2

Knoll, A. H., & Calder, S. (1983). Microbiotas of the late Precambrian Ryssö formation, Nordaustlandet, Svalbard. *Palaeontology*, *26*(3), 467–496.

Knoll, A. H., Swett, K., & Mark, J. (1991). Paleobiology of a Neoproterozoic tidal flat/lagoonal complex: The Draken Conglomerate Formation, Spitsbergen. *Journal of Paleontology*, *65*(4), 531–570.

Kraskov, L. N. (1985). Находка проблематических организмов в отложениях Чаткарагайскоа свиты (Таласский хребет) (finding of problematic organisms in sediments of Chatkaragai suite (Talas ridge)). *Академии наук СССР, Трудьі (USSR Academy of Sciences, Proceedings)*, *632*, 149–152.

Lahr, D. J., Bosak, T., Lara, E., & Mitchell, E. A. (2015). The phanerozoic diversification of silica-cycling testate amoebae and its possible links to changes in terrestrial ecosystems. *PeerJ*, *3*, e1234. https://doi.org/10.7717/peerj.1234

Lahr, D. J., Kosakyan, A., Lara, E., Mitchell, E. A., Morais, L., Porfirio-Sousa, A. L., Ribeiro, G. M., Tice, A. K., Pánek, T., Kang, S., & Brown, M. W. (2019). Phylogenomics and morphological reconstruction of Arcellinida testate amoebae highlight diversity of microbial eukaryotes in the Neoproterozoic. *Current Biology*, *29*(6), 991–1001. https://doi.org/10.1016/j.cub.2019.01.078

Lee, Y. C., Chiang, C. C., Huang, P. Y., Chung, C. Y., Huang, T. D., Wang, C. C., Chen, C. I., Chang, R. S., Liao, C. H., & Reisz, R. R. (2017). Evidence of preserved collagen in an early Jurassic sauropodomorph dinosaur revealed by synchrotron FTIR microspectroscopy. *Nature Communications*, *8*, 14220. https://doi.org/10.1038/ncomms14220

Lillis, P. G. (2016). The Chuar petroleum system, Arizona and Utah. In *Hydrocarbon source rocks in unconventional plays*, *Rocky Mountain Region* (pp. 79–137). Rocky Mountain Association of Geologists. https://www.researchgate.net/profile/Paul-Lillis/publication/309313485_The_Chuar_Petroleum_System_Arizona_and_Utah/links/584c5f4208aecb6bd8c2e459/The-Chuar-Petroleum-System-Arizona-and-Utah.pdf

Liu, J., Xu, Z., & Masliyah, J. (2004). Role of fine clays in bitumen extraction from oil sands. *American Institute of Chemical Engineers Journal*, *50*, 1917–1927.

14724669, 0, Downloaded from https://onlinelibrary.wiley.com/doi/10.1111/gbi.12544 by University Of California, Santa Barbara, Wiley Online Library on [01/03/2023]. See the Terms and Conditions (https://onlinelibrary.wiley.com/terms-and-conditions) on Wiley Online Library for rules of use; OA articles are governed by the applicable Creative Commons License

Martí Mus, M., & Moczydłowska, M. (2000). Internal morphology and taphonomic history of the Neoproterozoic vase-shaped microfossils from the Visingsö Group, Sweden. *Norsk Geologisk Tidsskrift*, *80*, 213–228. https://doi.org/10.1080/002919600433751

Martí Mus, M., Moczydłowska, M., & Knoll, A. H. (2020). Morphologically diverse vase-shaped microfossils from the Russøya Member, Elbobreen Formation, in Spitsbergen. *Precambrian Research*, *350*, 105899. https://doi.org/10.1016/j.precamres.2020.105899

McNamara, M. E., Orr, P. J., Kearns, S. L., Alcalá, L., Anadón, P., & Peñalver-Mollá, E. (2006). High-fidelity organic preservation of bone marrow in ca. 10 ma amphibians. *Geology*, *34*(8), 641–644. https://doi.org/10.1130/G22526.1

McNamara, M. E., van Dongen, B. E., Lockyer, N. P., Bull, I. D., & Orr, P. J. (2016). Fossilization of melanosomes via sulfurization. *Palaeontology*, *59*(3), 337–350. https://doi.org/10.1111/pala.12238

Meisterfeld, R. (2000). Arcellinida. In J. J. Lee, G. F. Leedale, & P. Bradbury (Eds.), *Illustrated guide to the protozoa* (pp. 827–800). Society of Protozoologists.

Melendez, I., Grice, K., Trinajstic, K., Ladjavardi, M., Greenwood, P., & Thompson, K. (2013). Biomarkers reveal the role of photic zone euxinia in exceptional fossil preservation: An organic geochemical perspective. *Geology*, *41*(2), 123–126. https://doi.org/10.1130/G33492.1

Morais, L., Fairchild, T. R., Lahr, D. J., Rudnitzki, I. D., Schopf, J. W., Garcia, A. K., & Romero, G. R. (2017). Carbonaceous and siliceous Neoproterozoic vase-shaped microfossils (Urucum formation, Brazil) and the question of early protistan biomineralization. *Journal of Paleontology*, *91*(3), 393–406. https://doi.org/10.1017/jpa.2017.16

Morais, L., Freitas, B. T., Fairchild, T. R., Toniolo, T. F., Campos, M. D. R., Prado, G. M. E. M., Silva, P. A. S., Rudnitzki, I. D., Lahr, D. J. G., Leme, J. D. M., & Philippot, P. (2021). Diverse vase-shaped microfossils within a Cryogenian glacial setting in the Urucum Formation (Brazil). *Precambrian Research*, *367*, 106470. https://doi.org/10.1016/j.precamres.2021.106470

Morais, L., Lahr, D. J. G., Rudnitzki, I. D., Freitas, B. T., Romero, G. R., Porter, S. M., Knoll, A. H., & Fairchild, T. R. (2019). Insights into vase-shaped microfossil diversity and Neoproterozoic biostratigraphy in light of recent Brazilian discoveries. *Journal of Paleontology*, *93*(4), 612–627. https://doi.org/10.1017/jpa.2019.6

Myers, C. E., Bergmann, K. D., Sun, C. Y., Boekelheide, N., Knoll, A. H., & Gilbert, P. U. (2018). Exceptional preservation of organic matrix and shell microstructure in a late cretaceous *pinna* fossil revealed by photoemission electron spectromicroscopy. *Geology*, *46*(8), 711–714. https://doi.org/10.1130/G45271.1

Nagy, R. M., Porter, S. M., Dehler, C. M., & Shen, Y. (2009). Biotic turnover driven by eutrophication before the Sturtian low-latitude glaciation. *Nature Geoscience*, *2*(6), 415–418. https://doi.org/10.1038/ngeo525

Ogden, C. G. (1984). Shell structure of some testate amoebae from Britain (protozoa, Rhizopoda). *Journal of Natural History*, *18*(3), 341–361. https://doi.org/10.1080/00222938400770291

Ogden, G. G. (1988). Fine structure of the Shell Wall in the soil testate amoeba *Cyclopyxis kahli* (Rhizopoda). *The Journal of Protozoology*, *35*(4), 537–540. https://doi.org/10.1111/j.1550-7408.1988.tb04147.x

Olcott, A. N., Downen, M. R., Schiffbauer, J. D., & Selden, P. A. (2022). The exceptional preservation of Aix-En-Provence spider fossils could have been facilitated by diatoms. *Communications Earth & Environment*, *3*(1), 1–10. https://doi.org/10.1038/s43247-022-00424-7

Orr, P. J., Briggs, D. E., & Kearns, S. L. (1998). Cambrian burgess shale animals replicated in clay minerals. *Science*, *281*, 1173–1175. https://doi.org/10.1126/science.281.5380.1173

Porter, S. M., & Knoll, A. H. (2000). Testate amoebae in the Neoproterozoic era: Evidence from vase-shaped microfossils in the Chuar Group, Grand Canyon. *Paleobiology*, *26*(3), 360–385. https://doi.org/10.1666/0094-8373(2000)026%3C0360:TAITNE%3E2.0.CO;2

Porter, S. M., Meisterfeld, R., & Knoll, A. H. (2003). Vase-shaped microfossils from the Neoproterozoic Chuar Group, Grand Canyon: A classification guided by modern testate amoebae. *Journal of Paleontology*, *77*(3), 409–429. https://doi.org/10.1666/0022-3360(2003)077%3C0409:VMFTNC%3E2.0.CO;2

Porter, S. M., & Riedman, L. A. (2016). Systematics of organic-walled microfossils from the mid-Neoproterozoic Chuar Group, Grand Canyon, Arizona. *Journal of Paleontology*, *90*, 815–853. https://doi.org/10.1017/jpa.2016.57

Porter, S. M., & Riedman, L. A. (2019). Evolution: Ancient fossilized amoebae find their home in the tree. *Current Biology*, *29*(6), R212–R215. https://doi.org/10.1016/j.cub.2019.02.003

Rasmussen, B., & Muhling, J. R. (2019). Organic-rich microfossils produced by oil infiltration of hollow silicified bacteria: Evidence from the ca. 340 ma red dog Zn-Pb deposit, Alaska. *Geology*, *47*, 1107–1111. https://doi.org/10.1130/G46346.1

Rasmussen, B., Muhling, J. R., & Fischer, W. W. (2021). Ancient oil as a source of carbonaceous matter in 1.88-billion-year-old gunflint stromatolites and microfossils. *Astrobiology*, *21*(9), 1–18. https://doi.org/10.1089/ast.2020.2376

Raven, M. R., Fike, D. A., Gomes, M. L., Webb, S. M., Bradley, A. S., & McClelland, H. L. O. (2018). Organic carbon burial during OAE2 driven by changes in the locus of organic matter sulfurization. *Nature Communications*, *9*(1), 1–9. https://doi.org/10.1038/s41467-018-05943-6

Raven, M. R., Keil, R. G., & Webb, S. M. (2021). Microbial sulfate reduction and organic sulfur formation in sinking marine particles. *Science*, *371*(6525), 178–181. https://doi.org/10.1126/science.abc6035

Riedman, L. A., Porter, S. M., & Calver, C. R. (2018). Vase-shaped microfossil biostratigraphy with new data from Tasmania, Svalbard, Greenland, Sweden and the Yukon. *Precambrian Research*, *319*, 19–36. https://doi.org/10.1016/j.precamres.2017.09.019

Riedman, L. A., Porter, S. M., & Czaja, A. D. (2021). Phosphatic scales in vase-shaped microfossil assemblages from Death Valley, Grand Canyon, Tasmania, and Svalbard. *Geobiology*, *19*, 364–375. https://doi.org/10.1111/gbi.12439

Rooney, A. D., Austermann, J., Smith, E. F., Li, Y., Selby, D., Dehler, C. M., Schmitz, M. D., Karlstrom, K. E., & Macdonald, F. A. (2018). Coupled Re-Os and U-Pb geochronology of the Tonian Chuar Group, Grand Canyon. *Geological Society of America Bulletin*, *130*, 1085–1098. https://doi.org/10.1130/B31768.1

Saito, Y., Tiba, T., & Matsubara, S. (1988). Precambrian and Cambrian cherts in northwestern Tasmania. *Bulletin of the National Science Museum*, *14*(2), 59–70.

Schiffbauer, J. D., Xiao, S., Cai, Y., Wallace, A. F., Hua, H., Hunter, J., Xu, H., Peng, Y., & Kaufman, A. J. (2014). A unifying model for Neoproterozoic–Palaeozoic exceptional fossil preservation through pyritization and carbonaceous compression. *Nature Communications*, *5*(1), 1–12. https://doi.org/10.1038/ncomms6754

Schopf, J. W., Ford, T. D., & Breed, W. J. (1973). Microorganisms from the late Precambrian of the Grand Canyon, Arizona. *Science*, *179*(4080), 1319–1321.

Sergeev, V. N., & Schopf, J. W. (2010). Taxonomy, paleoecology and biostratigraphy of the late Neoproterozoic Chichkan microbiota of South Kazakhstan: The marine biosphere on the eve of metazoan radiation. *Journal of Paleontology*, *84*(3), 363–401. https://doi.org/10.1666/09-133.1

Sinninghe Damsté, J. S., & De Leeuw, J. W. (1987). The origin and fate of isoprenoid C20 and C15 sulphur compounds in sediments and oils. *International Journal of Environmental Analytical Chemistry*, *28*, 1–19. https://doi.org/10.1080/03067318708078398

Sinninghe Damsté, J. S., & De Leeuw, J. W. (1990). Analysis, structure and geochemical significance of organically-bound sulphur in the

14724669, 0, Downloaded from https://onlinelibrary.wiley.com/doi/10.1111/gbi.12544 by University Of California, Santa Barbara, Wiley Online Library on [01/03/2023]. See the Terms and Conditions (https://onlinelibrary.wiley.com/terms-and-conditions) on Wiley Online Library for rules of use; OA articles are governed by the applicable Creative Commons License

geosphere: State of the art and future research. *Organic Geochemistry*, *16*, 1077–1101. https://doi.org/10.1016/0146-6380(90)90145-P

Strauss, J. V., Rooney, A. D., Macdonald, F. A., Brandon, A. D., & Knoll, A. H. (2014). 740 ma vase-shaped microfossils from Yukon, Canada: Implications for Neoproterozoic chronology and biostratigraphy. *Geology*, *42*(8), 659–662. https://doi.org/10.1130/G35736.1

Summons, R. E., Brassell, S. C., Eglinton, G., Evans, E., Horodyski, R. J., Robinson, N., & Ward, D. M. (1988). Distinctive hydrocarbon biomarkers from fossiliferous sediment of the late Proterozoic Walcott member, Chuar Group, Grand Canyon, Arizona. *Geochimica et Cosmochimica Acta*, *52*, 2625–2637. https://doi.org/10.1016/0016-7037(88)90031-2

Timmons, J. M., Karlstrom, K. E., Dehler, C. M., Geissman, J. W., & Heizler, M. T. (2001). Proterozoic multistage (ca. 1.1 and 0.8 Ga) extension recorded in the grand canyon supergroup and establishment of northwest-and north-trending tectonic grains in the southwestern United States. *Geological Society of America Bulletin*, *113*(2), 163–181. https://doi.org/10.1130/0016-7606(2001)113<0163:PMCAGE>2.0.CO;2

Timmons, J. M., Karlstrom, K. E., Heizler, M. T., Bowring, S. A., Gehrels, G. E., & Crossey, L. J. (2005). Tectonic inferences from the ca. 1255–1100 ma Unkar Group and Nankoweap Formation, Grand Canyon: Intracratonic deformation and basin formation during protracted Grenville orogenesis. *GSA Bulletin*, *117*(11–12), 1573–1595. https://doi.org/10.1130/B25538.1

Van Gundy, C. E. (1951). Nankoweap Group of the Grand Canyon Algonkian of Arizona. *Geological Society of America Bulletin*, *62*(8), 953–959. https://doi.org/10.1130/0016-7606(1951)62[953:NGOTGC]2.0.CO;2

Vidal, G. (1979). Acritarchs from the upper Proterozoic and lower Cambrian of East Greenland. *Grønlands Geologiske Undersøgelse*, *134*, 1–40.

Vidal, G., & Ford, T. D. (1985). Microbiotas from the late Proterozoic Chuar Group (northern Arizona) and Uinta Mountain Group (Utah) and their chronostratigraphic implications. *Precambrian Research*, *28*(3–4), 349–389.

Wacey, D., Saunders, M., Roberts, M., Menon, S., Green, L., Kong, C., Culwick, T., Strother, P., & Brasier, M. D. (2014). Enhanced cellular preservation by clay minerals in 1 billion-year-old lakes. *Scientific Reports*, *4*, 1–11.

Walcott, C. D. (1899). Precambrian fossiliferous formations. *Geological Society of America Bulletin*, *10*, 199–244. https://doi.org/10.1130/GSAB-10-199

Wang, C., Lechte, M. A., Reinhard, C. T., Asael, D., Cole, D. B., Halverson, G. P., Porter, S. M., Galili, N., Halevy, I., Rainbird, R. H., & Lyons, T. W. (2022). Strong evidence for a weakly oxygenated ocean–atmosphere system during the Proterozoic. *Proceedings of the National Academy of Sciences*, *119*(6), e2116101119. https://doi.org/10.1073/pnas.2116101119

Webb, S. M. (2005). SIXpack: A graphical user interface for XAS analysis using IFEFFIT. In *AIP 919 conference proceedings*. 1011. https://doi.org/10.1063/1.3625338

Webb, S. M., McNulty, I., Eyberger, C., & Lai, B. (2011). The MicroAnalysis toolkit: X-ray fluorescence image processing software. In *10th International conference on X-ray microscopy* (pp. 196–199). https://doi.org/10.1238/Physica.Topical.115a01011

Weil, A. B., Geissman, J. W., & Van der Voo, R. (2004). Paleomagnetism of the Neoproterozoic Chuar group, grand canyon supergroup, Arizona: Implications for Laurentia's Neoproterozoic APWP and Rodinia breakup. *Precambrian Research*, *129*, 71–92. https://doi.org/10.1016/j.precamres.2003.09.016

Werne, J. P., Hollander, D. J., Lyons, T. W., & Damsté, J. S. S. (2004). Organic sulfur biogeochemistry: Recent advances and future research directions. *Geological Society of America Special Papers*, *379*, 135–150. https://doi.org/10.1130/0-8137-2379-5.135

Werne, J. P., Lyons, T. W., Hollander, D. J., Schouten, S., Hopmans, E. C., & Damsté, J. S. S. (2008). Investigating pathways of diagenetic organic matter sulfurization using compound-specific sulfur isotope analysis. *Geochimica et Cosmochimica Acta*, *72*(14), 3489–3502. https://doi.org/10.1016/j.gca.2008.04.033

Wiemann, J., Crawford, J. M., & Briggs, D. E. (2020). Phylogenetic and physiological signals in metazoan fossil biomolecules. *Science Advances*, *6*, eaba6883. https://doi.org/10.1126/sciadv.aba6883

Woltz, C. R., Porter, S. M., Agić, H., Dehler, C. M., Junium, C. K., Riedman, L. A., Hodgskiss, M. S. W., Wörndle, S., & Halverson, G. P. (2021). Total organic carbon and the preservation of organic-walled microfossils in Precambrian shale. *Geology*, *49*(5), 556–560. https://doi.org/10.1130/G48116.1

Zolotov, M. Y., & Shock, E. L. (2005). Formation of jarosite-bearing deposits through aqueous oxidation of pyrite at Meridiani Planum, Mars. *Geophysical Research Letters*, *32*(21), L21203. https://doi.org/10.1029/2005GL024253

Zumberge, J. A., Rocher, D., & Love, G. D. (2019). Free and kerogen-bound biomarkers from late Tonian sedimentary rocks record abundant eukaryotes in mid-Neoproterozoic marine communities. *Geobiology*, *18*(3), 326–347. https://doi.org/10.1111/gbi.12378

SUPPORTING INFORMATION

Additional supporting information can be found online in the Supporting Information section at the end of this article.

How to cite this article: Tingle, K. E., Porter, S. M., Raven, M. R., Czaja, A. D., Webb, S. M., & Bloeser, B. (2023). Organic preservation of vase-shaped microfossils from the late Tonian Chuar Group, Grand Canyon, Arizona, USA. *Geobiology*, *00*, 1–20. https://doi.org/10.1111/gbi.12544

14724669, 0, Downloaded from https://onlinelibrary.wiley.com/doi/10.1111/gbi.12544 by University Of California, Santa Barbara, Wiley Online Library on [01/03/2023]. See the Terms and Conditions (https://onlinelibrary.wiley.com/terms-and-conditions) on Wiley Online Library for rules of use; OA articles are governed by the applicable Creative Commons License